INFORMATION TO USERS

This manuscript has been reproduced from the microfilm master. UMI films the text directly from the original or copy submitted. Thus, some thesis and dissertation copies are in typewriter face, while others may be from any type of computer printer.

The quality of this reproduction is dependent upon the quality of the copy submitted. Broken or indistinct print, colored or poor quality illustrations and photographs, print bleedthrough, substandard margins, and improper alignment can adversely affect reproduction.

In the unlikely event that the author did not send UMI a complete manuscript and there are missing pages, these will be noted. Also, if unauthorized copyright material had to be removed, a note will indicate the deletion.

Oversize materials (e.g., maps, drawings, charts) are reproduced by sectioning the original, beginning at the upper left-hand corner and continuing from left to right in equal sections with small overlaps.

ProQuest Information and Learning
300 North Zeeb Road, Ann Arbor, MI 48106-1346 USA
800-521-0600

UMI®

University of Alberta

INTERNAL WAVE GENERATION FROM STRATIFIED FLOW OVER
FINITE-AMPLITUDE PERIODIC TOPOGRAPHY

by

Dawn A. Aguilar ©

A thesis submitted to the Faculty of Graduate Studies and Research in partial
fulfillment of the requirements for the degree of **Master of Science.**

in

Applied Mathematics

Department of Mathematical and Statistical Sciences

Edmonton, Alberta
Fall 2005

Library and
Archives Canada

Bibliothèque et
Archives Canada

0-494-09110-X

Published Heritage
Branch

Direction du
Patrimoine de l'édition

395 Wellington Street
Ottawa ON K1A 0N4
Canada

395, rue Wellington
Ottawa ON K1A 0N4
Canada

Canada

Abstract

Laboratory experiments are performed to study internal wave generation from finite-amplitude periodic topography. Model hills of varying steepness are towed at constant speeds along the surface of a uniformly salt-stratified fluid. The experiments show that internal waves are generated not only by flow over the hills but also by flow over "boundary-trapped" lee waves and by vigorous turbulence created in the lee of steep hills. Waves are visualized and their characteristics measured using the non-intrusive optical technique, "synthetic schlieren". Experimental results are compared with the predictions of linear theory and Long's model. For low values of the excitation frequency, linear theory predicts well the internal wave frequencies but significantly overestimates the wave amplitudes. This indicates the importance of nonlinear processes such as boundary layer separation. When the excitation frequency exceeds the buoyancy frequency, turbulence is created and results in the excitation of internal waves within a narrow frequency range.

Acknowledgements

I would first of all like to thank God for giving me the abilities, strength, and motivation to complete this task, for *"I can do all things through Christ who strengthens me."*- Philippians 4:13

A close second is my family, especially my husband, Cesar, and my twin sister, Tara, who are my biggest cheerleaders. My family has always been supportive, encouraging, and genuinely excited about all of my endeavors, including my research. I am so richly blessed to have such a wonderful family and I dedicate this thesis to each member.

One cannot perform quality research without a quality supervisor and I was fortunate to have one of the best. The qualities that make Bruce a good supervisor include his passion for his research, his interest in his students' work, and his willingness to help and give direction while at the same time allow his students to explore on their own.

Finally, I would like to thank my friends and colleagues for helping to make my time here more meaningful and enjoyable.

Table of Contents

List of Tables

List of Figures

Chapter 1

Introduction

1.1   Motivation

The study of fluid motion past obstacles of various shapes is one of the principal topics in the study of classical fluid mechanics. If the flow is sufficiently fast or the obstacle sufficiently rough, then a turbulent wake may form in the lee of the obstacle. If the fluid is stratified, meaning that its density changes with height, the problem becomes increasingly complex. In particular, internal waves may be generated as the fluid flows over the obstacle. Furthermore, in the case where turbulence is created near the obstacle, the turbulence may itself contribute to wave generation. The purpose of this study is to use laboratory experiments to increase our understanding beyond the limitations of existing theory of internal wave generation from finite-amplitude topography.

In general, internal waves are generated whenever a stratified fluid is perturbed at a frequency below the natural frequency of vertical oscillation of the fluid (i.e. the buoyancy frequency). The waves subsequently propagate horizontally and vertically within the fluid, transporting energy and momentum away from their source. Eventually, waves may become unstable and break, depositing momentum and energy to the background flow.

The flow of air over mountain ranges or tides over the rough terrain of the ocean floor are important examples of environmental stratified flows over

1

obstacles. In the atmosphere, internal waves launched by air flow over mountains can greatly affect the mean winds and thus, the general circulation of the atmosphere (McFarlane, 1987; McLandress, 1998). It is therefore important to understand the complex interaction between the flow and rough terrain in order to (i) obtain improved weather and climate predictions, (ii) reliably predict the transport and dispersion of pollutants over complex terrain, and (iii) provide predictions which are sufficiently precise to maximize the safety of aircraft traversing mountainous regions (Boyer and Srdic-Mitrovic, 2002). Another source of internal waves in the atmosphere, about which much less is known, is the sudden formation of turbulent patches by a dynamical instability (Staquet and Sommeria, 2002). Since turbulence may be generated by flow over rough topography, it is of interest to study the interaction between turbulence and internal waves.

In the ocean, internal waves are a significant source of mixing, which consequently redistributes heat and so may influence the Earth's climate (Ledwell et al., 2000; Rudnick et al., 2003). Recent observations in the deep-ocean have shown that waves are generated most significantly by the flow of tides over the rough terrain of the ocean floor, such as sea mounts, ridges, and canyons (New and DaSilva, 2002; Rudnick et al., 2003; St. Laurent et al., 2003). In many of these sites, energetic turbulence has been observed (Ledwell et al., 2000; Klymak and Gregg, 2004; Garabato et al., 2004) and presumably results directly as a consequence of flow over topography and wave breaking. Internal waves may also be excited just below the ocean's surface by wind stress fluctuations, which randomly deform the base of the surface mixed layer (see for example, Skyllingstad and Denbo, 1994).

The characteristics of the internal wave field generated by tidal flows over bottom topography depend on the observation time scale, as depicted in the schematic of Figure 1.1. When tidal flows are observed on scales well above

2

the inertial period, f^{-1}, (e.g. days and/or months), the waves radiate mainly at the fundamental frequency of the tide in both upstream and downstream directions. However, when the flows are observed over intermediate time-scales close to the buoyancy period, N^{-1}, (e.g. minutes and/or hours), the flow resembles uniform flow over topography and the waves propagate only in the upstream direction with phase speed $\sim U$ and frequency $\sim Uk$ relative to the topography. Here, U is the tidal flow speed, k^{-1} is the horizontal length scale of the topography, and N is the buoyancy frequency, given in terms of the background density, $\bar{\rho}(z)$, a characteristic density, ρ_0, and the acceleration due to gravity, g, by (A.16). On very fast time scales, the small-scale processes, such as turbulence generated by flow over rough topography, can be observed.

Another parameter used in classifying flow over bottom topography is the steepness parameter, $\epsilon = s/\alpha$. Here s is the topographic slope defined as the ratio of the topographic height to length, $s = Hk$, and α is the slope of the wave beam, defined as the ratio of the horizontal to vertical wavenumbers, $\alpha = k_x/k_z$. Topography is termed "subcritical" if $\epsilon < 1$ and "supercritical" if $\epsilon > 1$.

Much attention has been devoted to the "internal tide" regime (Figure 1.1a) using both subcritical and supercritical topography (e.g. recently by Llewellyn Smith and Young, 2002; Balmforth et al., 2002; St. Laurent and Garrett, 2002). Even so, the properties of internal tides generated at supercritical topography remain poorly understood (St. Laurent et al., 2003). Here, we discuss the situation depicted in Figure 1.1b,c in which non-hydrostatic waves are generated from steady flow over both subcritical and supercritical topography. In such cases, the mechanisms by which internal waves are generated from topography are poorly understood beyond the suppositions of linear and inviscid theories.

3
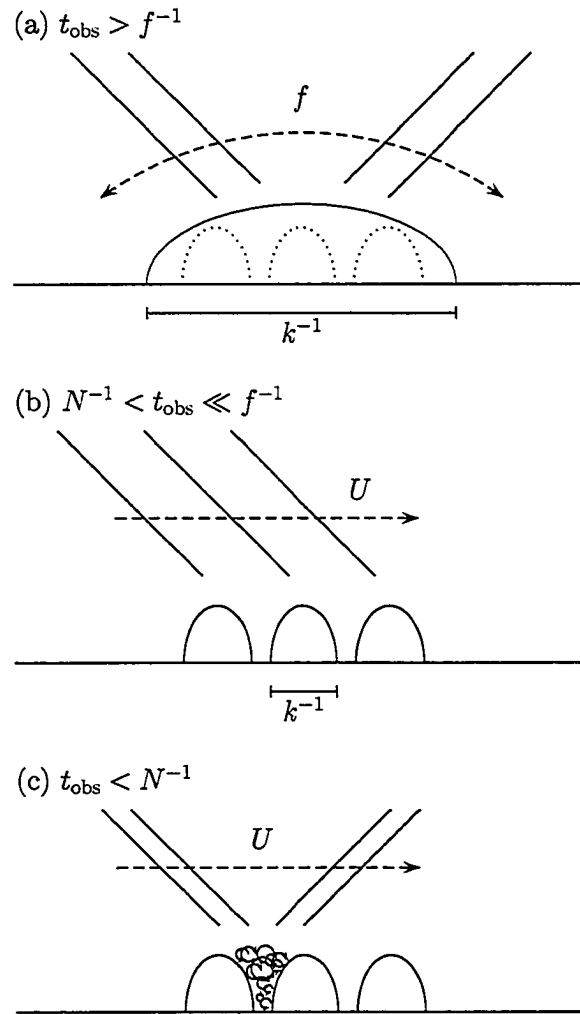
Figure 1.1: Different time scales for observations of wave fields (adapted from Dohan, 2004): (a) On time scales longer than the inertial period, tidal motion can be viewed as periodic and generates internal waves at approximately the fundamental frequency of the tides. (b) On time scales less than the inertial period, tidal motion can be viewed locally as uniform flow over topography, with internal waves generated only in the upstream direction. (c) On time scales less than the buoyancy period, small-scale turbulent processes can be observed.

1.2 Theory

Linear theory restricts predictions of topographically-generated waves to those launched by smooth hills with small aspect ratios of topographic height to width, H/L. In such cases, theory predicts that propagating waves will be generated if the excitation frequency, ω_{exc}, is lower than the buoyancy frequency, N. Here, ω_{exc} is defined in terms of the flow speed, U, and the topographic width, L, (for example, $L = \lambda$ for sinusoidal topography) as

$$\omega_{exc} \equiv U\frac{2\pi}{L} = Uk. \qquad (1.1)$$

The ratio of excitation to buoyancy frequency defines a "horizontal" Froude number,

$$\mathrm{Fr}_h \equiv \frac{\omega_{exc}}{N} = \frac{Uk}{N}. \qquad (1.2)$$

Thus linear theory predicts that vertically-propagating internal waves are generated if $\mathrm{Fr}_h < 1$ (subcritical flow), in which case the maximum vertical displacement, A_ξ, of the fluid due to waves equals $H/2$, half the peak-to-peak height of the hills. When $\mathrm{Fr}_h > 1$ (supercritical flow), the waves are termed "evanescent" meaning that the wave amplitude decays exponentially. Fr_h also provides a measure of hydrostatic balance. In particular the flow is hydrostatic if $\mathrm{Fr}_h \ll 1$.

In addition to Fr_h, an equally important parameter for studying stratified flow over topography is the quantity NH/U, which is used as a measure of nonlinearity introduced by a finite topographic height. There is no standard symbol for this quantity in the literature and thus, in this report, we will define a "vertical" Froude number by,

$$\mathrm{Fr}_v^{-1} \equiv \frac{NH}{U}. \qquad (1.3)$$

Combining these two parameters gives $\mathrm{Fr}_h\mathrm{Fr}_v^{-1} = Hk$. Thus, the linear theory assumption can be summarized by the condition that $Hk \ll 1$. In

5

the ocean, this is valid, for example, to describe tidal flow over mid-ocean ridge topography with subcritical slopes and occurring on long time scales (Balmforth et al., 2002). However, it is not valid when modeling flow associated with supercritical oceanic trench systems, such as the Hawaiian and Aleutian ridges (St. Laurent et al., 2003), or mountain ranges such as the Andes or Rockies. It is therefore important to understand the limitations of applying results from linear theory to such circumstances. This study will specifically examine the cases of $Hk = 0.6$ and 1.2 on time scales close to the buoyancy period.

Long's model (Long, 1953) extends linear theory to include waves generated by steady, inviscid flow over finite-amplitude topography, which does not include the nonlinear dynamics of boundary layer separation from steep slopes, flow stagnation in valleys, and turbulence. In real situations, such nonlinear and unsteady effects can act to alter the generation of internal waves. The purpose of the present research is to use laboratory experiments to investigate the ways in which internal waves are generated from flow over and in the lee of finite-amplitude topography, including the nonlinear effects described above, and to determine the corresponding limitations of linear and inviscid theories.

1.3 Background

Boundary layer separation occurs when fluid flowing over an obstacle encounters an adverse pressure gradient, which decelerates the fluid and causes the boundary layer to separate from the obstacle. In the context of flow over topography, this can occur on the lee-side slopes of both isolated and periodic hills provided that the flow is sufficiently energetic and/or the hills sufficiently steep.

According to Baines (1995), separation should occur for $NL_h/U < \pi$ ($\mathrm{Fr}_h >$ 1) and complete attachment for $NL_h/U > \pi$ ($\mathrm{Fr}_h < 1$), where L_h is the

6

half-width of the obstacle (whether isolated or part of a range). However, separation can still occur at lower Fr_h values, provided that Fr_v^{-1} and H/L are sufficiently high. This will be of particular interest in our experiments, which have relatively large values of H/L and $Fr_v^{-1} \sim 1$. We hypothesize that for experiments with tall and rough topography, boundary layer separation will eventually become independent of Fr_h, being controlled predominately by Fr_v^{-1}.

When fluid separates from the lee-side slope of an isolated hill (or the last in a range of hills), the formation of a stationary, undulating shear layer downstream of the hill, sometimes called a "boundary-trapped" lee wave, may result. This is an example of what Baines (1995) calls "post-wave" separation. Beneath the crests of the lee waves lies either stagnant or mixed fluid, depending on the flow speed. Flow over these "fluidic" hills has been identified as a possible mechanism of internal wave generation (Sutherland, 2002).

Laboratory experiments performed by Sutherland (2002) examined stratified flow over a "smooth" step and showed that vertically-propagating internal waves and boundary-trapped lee waves were generated with frequency a constant fraction of the buoyancy frequency, approximately $0.75N$ for $Fr_v^{-1} < 1$ and moderately smaller values for larger Fr_v^{-1}. Sutherland observed that the generation of propagating internal waves was coupled to that of boundary-trapped lee waves and suggested that this may be an important factor in mixing over rough topography in the ocean. This study did not, however, capture the dynamics of the flow of fluid into and out of the valleys of topographic features such as mountain ridges on land or sea mounts and canyons on the ocean floor. The present research is thus an extension of this work to include the more complex dynamics of flow over, between, and in the lee of finite-amplitude periodic topography.

In the case of periodic topography, through boundary layer separation,

7

stagnant fluid may remain trapped within the valleys. The formation of stagnant fluid thus reduces the effective overall hill height for wave generation. The depth of these "blocked layers" increases slightly with increasing Fr_v^{-1} (Baines, 1995). Using numerical simulations, Welch et al. (2001) examined the formation and properties of blocked layers between finite-amplitude sinusoidal hills. They found that blocked layers were formed when Fr_v^{-1} exceeded a certain threshold, between 0.5 and 1. Also, once the hill height reached a certain threshold, the height of the blocked layer was found to increase linearly with H so as to achieve a relatively constant effective hill height, H_{eff}. The constancy of H_{eff} suggested that flow with background N and U could only sustain waves of a certain amplitude.

Turbulence above and in the lee of periodic topography may be created if the flow speed is sufficiently high and the topography sufficiently steep. There have been relatively few studies of turbulence (coherent or random) as a generation mechanism of internal waves (Linden, 1975; Carruthers and Hunt, 1986; Dohan and Sutherland, 2003). In a recent adaption of experiments by Linden (1975), Dohan and Sutherland (2003) examined the excitation of internal waves from random small-scale turbulent forcing above a stationary stratified fluid. Despite the random nature of the forcing, the resulting wave frequencies were found to lie within a narrow range. This same result was found in corresponding two-dimensional numerical simulations (Dohan, 2004).

Sutherland and Linden (1998) performed laboratory experiments to investigate the excitation of internal waves from a turbulent shear flow over a thin barrier. In their study, a coupling was observed between coherent turbulent structures shed in the lee of the barrier and the internal waves that radiated from the mixing region. In particular, internal waves were observed to propagate with the same length-scale and horizontal phase speed as disturbances at the base of the mixing region. Part of the work presented here extends

8

the research on turbulence generation to examine the situation of supercritical flow over rough topography and to determine the effects of turbulence created in the lee of topography on wave generation.

1.4 Thesis Overview

The organization of this report is as follows: Chapter 2 introduces the experimental set-up, including methods for wave visualization and techniques for determining wave properties such as frequency, wavenumber and amplitude. In Chapter 3, the results of the experiments using sinusoidal topography are presented. The properties of the waves are presented as a function of topographic height and flow speed and are compared with the predictions of linear theory and Long's model. Qualitative images of the flow near and in the lee of the hills are used to help explain the results.

Chapter 4 presents the results using rough topography, in particular rectangular and triangular hills, which are compared with those of Chapter 3. Flow over these steep topographic slopes results in the generation of a turbulent mixed region far in the lee of the topography, not present in the sinusoidal hill experiments. The effect of this turbulent region on wave generation is discussed. Chapter 5 concludes the study with a summary of significant findings, which have applications in both the atmosphere and ocean.

Appendix A develops the theory of linear internal waves. The section begins with the governing equations of fluid motion, then describes the important assumptions and simplifications relevant to our study, and concludes by giving equations for the fundamental properties of linear internal waves such as the the dispersion relation. Readers unfamiliar with fluid dynamics and internal waves may find it helpful to begin with this material. A derivation of Long's model, including solution techniques, is given in Appendix B.

9

Chapter 2

Experimental Methods

2.1 Introduction

This section gives a detailed description of the laboratory experiments performed for this study. A subsection is devoted to describing the relatively new experimental technique "synthetic schlieren", which is used to visualize and indirectly measure wave amplitudes. Analysis techniques, including the use of time series to determine quantitative values of internal wave frequency, wavenumber, and amplitude are also discussed. All illustrative examples in this chapter are taken from an experiment using the large-amplitude sinusoidal hills towed at a moderate speed, hereafter referred to as the featured experiment.

2.2 Apparatus

Experiments were performed in a glass tank having dimensions 197 cm long by 50 cm high by 17.5 cm wide. The tank was filled with uniformly salt-stratified water to a depth of approximately 27 cm. This was accomplished using the standard "double-bucket" technique (Oster, 1965). The background density field, $\bar{\rho}(z)$, was obtained by traversing a conductivity probe down through the tank before each experiment. A schematic illustrating the tank dimensions and a typical background density profile is given in Figure 2.1a. The buoyancy

10

frequency was determined directly from the slope of the best-fit line to the density profile. With some exceptions, its typical value was $N = 1.10 \pm 0.02\,\text{s}^{-1}$.

Although the fluid had finite depth, the experiments were performed over such short periods of time ($\approx 30 - 80\,\text{s}$) that the vertically-propagating internal waves did not reach the tank bottom before the experiment finished. Thus, the effect of the bottom boundary was essentially negligible and the experiments effectively modeled wave propagation in an infinite-depth fluid.

Four model topographies of different shapes were used: two sinusoidal hills of different hill heights and triangular and rectangular hills. The topographic features, namely the total hill height, H, and the characteristic width, L, are summarized in Table 2.1. The relatively smooth sinusoidal hills were selected to determine the effect of finite H on linear theory predictions. In this report, the two model hills are referred to as "small-amplitude" and "large-amplitude". Note that the small-amplitude hills have relative hill height to width, $H/L = 0.1$, comparable with that of the Rocky Mountain ranges. The effect of shape and/or roughness was further explored using the tall and steep triangular and rectangular hills with $H/L = 0.2$. In these experiments, turbulence was created and played an important role in wave generation. All the model hills had the same length scale, L, and were spanwise uniform to model two-dimensional flow and wave generation.

To simulate uniform flow over topography, model hills were towed along the surface of the fluid at an approximately constant speed. This was achieved using a towing apparatus consisting of a motor, five pulleys, and a belt that was fixed to the model topography (see Figure 2.1a). The model hills were towed at speeds ranging from $U = 0.8$ - $5.2\,\text{cm/s}$. The corresponding horizontal and inverse vertical Froude numbers ranged from $\text{Fr}_h = 0.2$ - 2.1 and $\text{Fr}_v^{-1} = 0.29$ - 6.07.

Because the equations of fluid motion given in Appendix A are invariant

11

(a) Front view of tank and towing apparatus
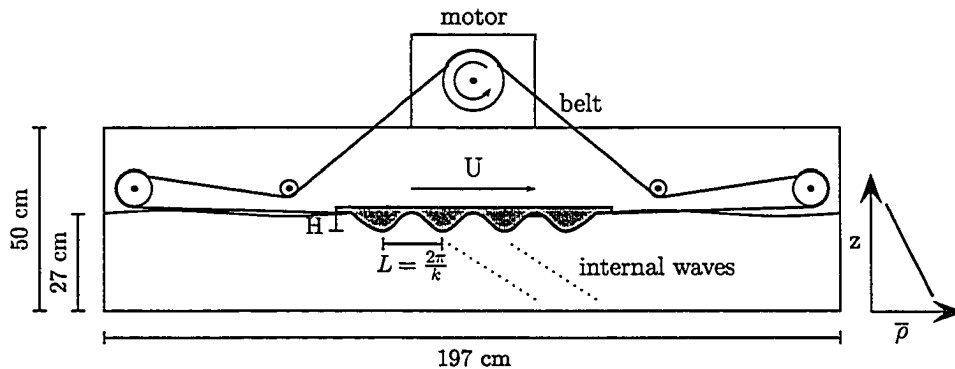
(b) Side view of synthetic schlieren set-up
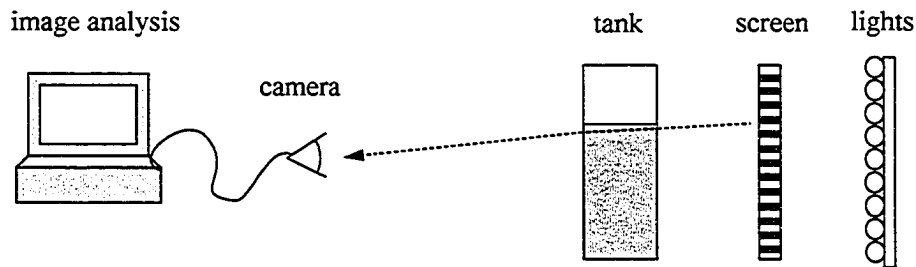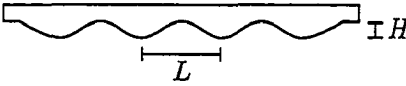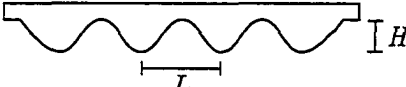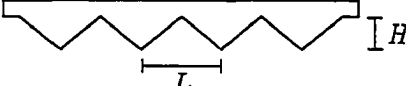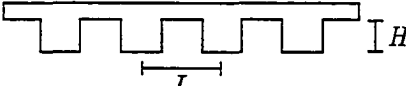
Figure 2.1: (a) Front view of tank and towing apparatus. The motor is mounted above the tank. A belt is attached to the topography and runs around a series of pulleys. When the motor is turned on, the topography moves from left to right at an approximately constant speed, thus exciting internal waves. (b) Side view of the experimental configuration for the synthetic schlieren technique. The technique records the distortion of the image of horizontal lines due to density fluctuations within the tank. The density fluctuations are the result of internal wave motion.

12

Table 2.1: Summary of model hills used in experiments

Description	Geometry	Length Scales
1. Small-amplitude Sinusoidal Hills	$\updownarrow H$ $\vdash\!\!-L-\!\!\dashv$	H=1.3 cm L=13.7 cm
2. Large-amplitude Sinusoidal Hills	$\updownarrow H$ $\vdash\!\!-L-\!\!\dashv$	H=2.6 cm L=13.7 cm
3. Triangular Hills	$\updownarrow H$ $\vdash\!\!-L-\!\!\dashv$	H=2.6 cm L=13.7 cm
4. Rectangular Hills	$\updownarrow H$ $\vdash\!\!-L-\!\!\dashv$	H=2.6 cm L=13.7 cm

under a Galilean transformation, the situations of fluid flowing at constant speed over stationary topography and towing topography at constant speed through stationary fluid are dynamically equivalent. Furthermore, because the density difference between the salt water at the top and bottom of the tank was small compared to the density of the water itself, the fluid was Boussinesq (see A.2, Page 83). Hence there is no dynamic difference between waves propagating downward from topography towed along the top of the tank and waves propagating upward from topography towed along the bottom of the tank.

Before the start of each experiment, potassium permanganate crystals were laid down in front of the topography, forming a straight vertical dye-line. The movement of the topography through the fluid produced a reverse background flow, which caused a net deceleration of the near-topography fluid. This background flow was clearly visualized by the movement of the dye-line from its original position (see for example Figure 2.3a,b). To determine whether or

13
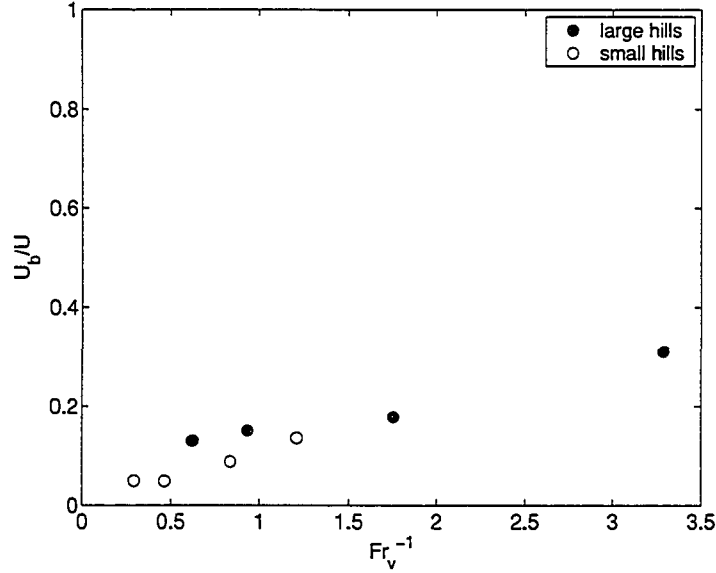
Figure 2.2: Plot of normalized background flow speed, U_b/U, as a function of Fr_v^{-1}. For most experiments, in which $\mathrm{Fr}_v^{-1} < 3$, the effect of the background flow is not significant. However, it may be important for experiments with large Fr_v^{-1}.

not the average background flow speed, U_b, was significant compared with the towing speed, it was approximated for eight experiments, covering a range of Fr_h and Fr_v^{-1}. This was done by measuring the average displacement of the dye-line over three hill periods. The results are given in Figure 2.2, which plots the background speed normalized by the towing speed as a function of Fr_v^{-1}. From the plot, the background flow speed was in most cases only 5 - 20 % of the towing speed, which is not high enough to have a significant effect on the results. However, for $\mathrm{Fr}_v^{-1} \gtrsim 3$, we found $U_b \gtrsim 0.3\,U$. In these extreme circumstances, the influence of the undercurrent should be taken into account when interpreting the results.

As Fr_h increased, the flow between and in the lee of the hills underwent a transition to turbulence. This altered the generation of waves from direct topographic generation to indirect turbulence generation, via both coherent turbulent structures and turbulent mixed regions.

14

The Reynolds number, based on L, ranged from $Re_L \approx 1000 - 5000$. Although significantly smaller than typical ocean and atmospheric values, $\sim 10^9$ and 10^{10} respectively, the experimental values are still large enough that viscous effects should be important only insofar as boundary layer separation and turbulence damping time scales are concerned. However, boundary layer separation occurs even for high Reynolds number geophysical flows and internal wave generation by turbulence is affected by integral length and time scales, not the viscous scales of turbulence. Therefore, the experimental results should be relevant to realistic circumstances in the atmosphere and ocean.

The experiments were recorded using a digital camera situated approximately 340 cm in front of the tank. The recorded images in the x-z plane were analyzed using the image processing software package, Digimage (Dalziel et al., 2000). The analysis of these images is described further in the following sections.

2.3 Synthetic Schlieren Technique

The synthetic schlieren technique was used to measure non-intrusively the two-dimensional internal wave field as it evolved in time (Dalziel et al., 2000). The technique is based on how light is deflected to a greater or lesser degree as it passes respectively through stronger or weaker density gradients. The experimental configuration is illustrated schematically in Figure 2.1b.

A 50 cm long by 30 cm high translucent screen of horizontal black and white lines was placed behind the tank. Situated behind the screen was a bank of fluorescent lights, which illuminated the screen. The field-of-view of the camera was set such that a minimum of eight pixels covered the width of a single horizontal line. This generally resulted in a field-of-view measuring approximately 25 cm in the horizontal and 20 cm in the vertical, sufficiently large to capture the internal waves generated near the topography. A sample

15

field-of-view is given in Figure 2.3a, which shows an image taken immediately before the start of the featured experiment.

When internal waves move within the tank, they stretch and compress isopycnal surfaces, thereby changing the local density gradient. This consequently changes the local gradient of the index of refraction of the fluid so that the horizontal lines appear to be displaced. Figure 2.3b shows an image taken during the featured experiment, after the hills have been towed through a distance of one hill wavelength. The distortion of the horizontal lines compared to the initial image in Figure 2.3a is barely visible. By taking the difference between the images in Figure 2.3a,b, we obtain the qualitative synthetic schlieren image given in Figure 2.3c. The intensity difference between the images is multiplied by a factor of 2 to reveal clearly the regions having the greatest displacement, namely the wave crests and troughs.

By measuring the displacement of the lines from their initial position, $\Delta z(x, z, t)$, the change in the squared buoyancy frequency, due to the stretching and compression of isopycnal surfaces, can be directly calculated:

$$\Delta N^2(x, z, t) \equiv -\frac{g}{\rho_0}\frac{\partial \rho}{\partial z} \simeq \alpha \Delta z(x, z, t), \qquad (2.1)$$

where α is a constant that depends on the tank width, the distance from the tank to the screen, the indices of refraction of salt water and air, and the gravitational constant g (Sutherland et al., 1999). In our experiments, $\alpha = 6.5\,\mathrm{s}^{-2}\mathrm{cm}^{-1}$. A sample Δz field is shown in Figure 2.3d. Because (2.1) assumes disturbances across the tank are spanwise uniform, the computed wave field is reliable only away from the mixing near the hilltops.

From such images, the horizontal and vertical wavelengths can be estimated by measuring the horizontal and vertical distances between successive wave crests or troughs. For example, from Figure 2.3, $\lambda_x \approx 11\,\mathrm{cm}$ and $\lambda_z \approx 7\,\mathrm{cm}$, which correspondingly gives wavenumber components $k_x \approx 0.57\,\mathrm{cm}^{-1}$ and $k_z \approx$
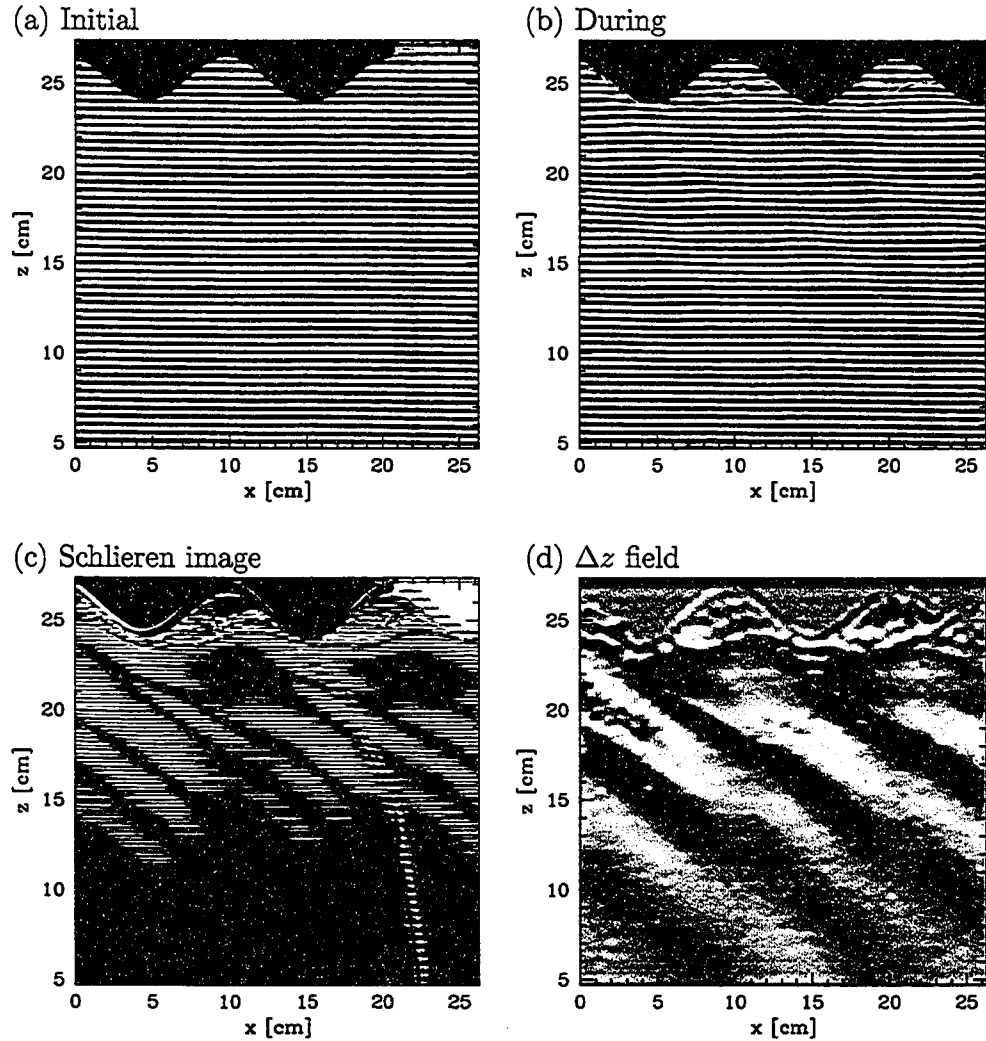
Figure 2.3: Snapshot images taken from the featured experiment (a) before the start of the experiment and (b) after the hills have been towed through a distance of one hill wavelength. Subtracting intensities in (a) from (b) and scaling yields the qualitative synthetic schlieren image (c). The corresponding Δz field is shown in (d), where the grey-scale range is between -0.08 and 0.08 cm. The vertical grey line at $x \simeq 22$ cm in (a) and the tilted line in (b) is the result of dye laid down by potassium permanganate crystals. This shows up as a vertical white streak in (c) but is filtered in computing Δz, as shown in (d). Parameter values for this experiment are $H = 2.6$ cm, $U = 0.97$ cm/s, $Fr_h = 0.41$, $Fr_v^{-1} = 2.94$, $Hk = 1.2$.

17

$0.90\,\mathrm{cm}^{-1}$. Rigorous quantitative methods for determining these quantities are presented in Section 3.3.1. Consequently, the angle of wave propagation to the vertical, Θ, (or equivalently, the angle formed by lines of constant phase with the vertical) can be estimated using the relation

$$\tan\Theta = \frac{k_z}{k_x}. \tag{2.2}$$

For this example, $\Theta \approx 58°$. Alternately, the angle can be estimated from the relative wave frequency using the dispersion relation (A.19).

In addition to calculating ΔN^2, the time-derivative of the squared buoyancy frequency, N_t^2, can be calculated by measuring the displacement of the horizontal lines between two short successive times. The time interval used in our experiments was $\Delta t = \frac{n}{30}\,\mathrm{s}$, where $n = 1,\ 2,\ 3,\ 4,$ or 5 depending on the towing speed. In all cases, Δt was much smaller than a typical wave period $(T \approx 10\,s)$, but large enough to give a substantial signal from the waves.

From the ΔN^2 field, the vertical and horizontal velocity fields can be estimated using linear theory. Similarly, the vertical displacement field, ξ, can be estimated from the N_t^2 field. These estimates are reasonable for small-amplitude disturbances up to $A_\xi/\lambda_x \approx 0.2$. For the purposes of performing qualitative and quantitative analyses, the N_t^2 field was preferred for three reasons: it was in phase with the vertical displacement field, ξ; it could be determined even for moderate-amplitude waves, which significantly distorted the background image; and it filtered long time-scale changes thus capturing the signal from propagating waves uncontaminated by the development of columnar modes.

2.4   Time Series Analyses

Time series of N_t^2 were used both to visualize the internal wave field and to determine quantitatively fundamental wave properties such as frequency,

18
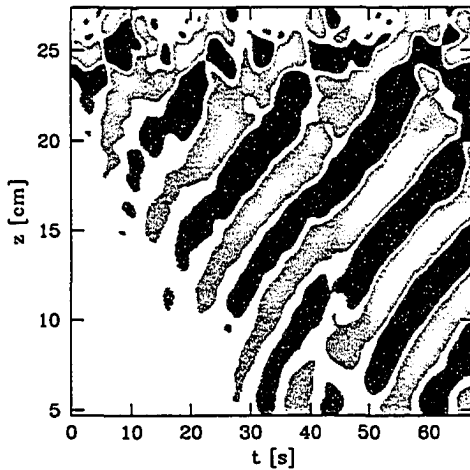
(a) Vertical   (b) Horizontal
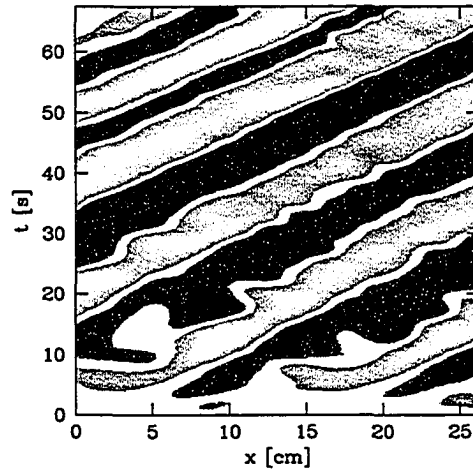
Figure 2.4: Sample (a) vertical and (b) horizontal time series of N_t^2 for the featured experiment. Time $t = 0\,\mathrm{s}$ corresponds to the start of towing. The vertical time series is taken at a horizontal location corresponding to the initial position of the first hill crest (at $x = 15\,\mathrm{cm}$ in Figure 2.3a). The horizontal time series is taken at a vertical location 5 cm below the hill crest. The light and dark bands are the wave crests and troughs, which move upwards and to the right as time evolves and the waves propagate downward and to the right. The grey-scale is arbitrary for the purpose of this figure.

19

wavenumber, and amplitude. Vertical time series, $N_t^2(z,t)$, illustrate the time evolution of a vertical slice through images of an experiment at a single horizontal location, whereas horizontal time series, $N_t^2(x,t)$, illustrate the time evolution of a horizontal slice at a single vertical location. Figure 2.4 shows sample vertical and horizontal time series for the featured experiment. Here, the horizontal time series has been reconstructed using 18 equally-spaced vertical time series images spanning the entire field-of-view. The images have been enhanced using low-pass filters to remove high frequency thermal and electronic noise and Fourier filters to remove low frequency thermal variations. From Figure 2.4a, lines of constant phase move upwards as times evolves, consistent with the linear theory prediction that energy is transported downwards and away from the hills. Figure 2.4b shows that the waves move from left to right, in the same direction toward which the topography is towed.

The frequencies and wavenumbers of the internal waves were determined from the peaks of the power spectra of the N_t^2 time series (see Section 3.3.1). The half peak-to-peak amplitude of the N_t^2 field, $A_{N_t^2}$, was determined by taking the root-mean-squared average in time and then multiplying by a factor of $\sqrt{2}$. For the purpose of making quantitative comparisons among experiments, a characteristic wave amplitude value was obtained by spatially averaging the root-mean-squared value. The averaging window was selected to isolate the waves and generally extended across a minimum of one wavelength in both directions, beginning at least 5 cm below the peak of the topography (see Section 3.3.1 for further details). This location was sufficiently far from the local mixing region where the schlieren technique did not accurately measure N_t^2. The amplitude of vertical displacement, A_ξ, was estimated from $A_{N_t^2}$ using the relation for Boussinesq linear plane waves in a uniformly stratified fluid, given

20

by

$$A_{N_t^2} = k_x N^3 \sin \Theta A_\xi,$$

$$= 2\pi N^3 \sqrt{1 - \text{Fr}_h^2} \frac{A_\xi}{\lambda_x} \tag{2.3}$$

in which Θ is given by (A.19) and Fr_h is given by (1.2).

21

Chapter 3

Results: Sinusoidal Topography

3.1 Introduction

In this section, we examine the results of the experiments performed using the small- and large-amplitude sinusoidal hills, as given in Table 2.1. The two sets of hills differ only in their hill height, H. One of the goals of this section is to determine the effect of hill height on both the resulting wave field and on the applicability of linear theory. The other is to examine the applicability of Long's inviscid, free-slip model to circumstances in which boundary layer separation may occur.

In this set of experiments, the model hills are towed at speeds ranging from $U = 0.88$ - 4.87 cm/s. The corresponding horizontal and inverse vertical Froude numbers range from $\mathrm{Fr}_h = 0.19$ - 2.03 and $\mathrm{Fr}_v^{-1} = 0.29$ - 6.07.

The process of boundary layer separation, both between the hills and in the lee, is examined using qualitative images of the near-hill region. For low values of Fr_h, separation is controlled largely by Fr_v^{-1} and acts to reduce the effective hill height for wave generation. For the large-amplitude hills, separation in the lee results in the formation of boundary-trapped lee waves. As Fr_h increases, the flow transitions to turbulence and coherent turbulent structures (also called boundary-trapped lee waves) are generated in the lee of both hills, although with significantly greater amplitude for the large-amplitude

22

hills. The formation of boundary-trapped lee waves, both at small and large Fr_h values, alters the generation of waves from direct topographic forcing to indirect generation via flow over the boundary-trapped lee waves.

This chapter begins with qualitative observations of representative experiments to gain an intuitive understanding of the dynamic processes involved. Following are quantitative results that summarize the wave properties for all experiments as a function of the horizontal Froude number and hill height. The results are compared with the predictions of linear theory and Long's model.

3.2 Qualitative Observations

3.2.1 Internal Wave Fields

Much insight into the mechanisms of internal wave generation over sinusoidal topography can be gained by comparing the visual wave fields for different parameter values. Recall that when the towing speed, U, is sufficiently small, i.e. $Fr_h < 1$, linear theory predicts the generation of propagating internal waves and the waves are evanescent otherwise. For linear theory to be valid, we require both $Fr_v^{-1} \ll 1$ and $Hk = Fr_h/Fr_v \ll 1$. Figure 3.1 summarizes the experiments we have performed in terms of Fr_h and Fr_v^{-1}. We have focused on the weakly ($Fr_v^{-1} \lesssim 1$) and strongly ($Fr_v^{-1} > 1$) nonlinear regime because it lies beyond well-established theory and because for very small-amplitude hills, the generated internal waves are too small to be accurately measured above signal noise.

To illustrate the properties of internal waves as they depend on towing speed and topographic height, we compare four vertical time series of N_t^2. Two are taken from experiments using the small-amplitude hills and two from those using the large-amplitude hills (Figure 3.2). The vertical time series

23
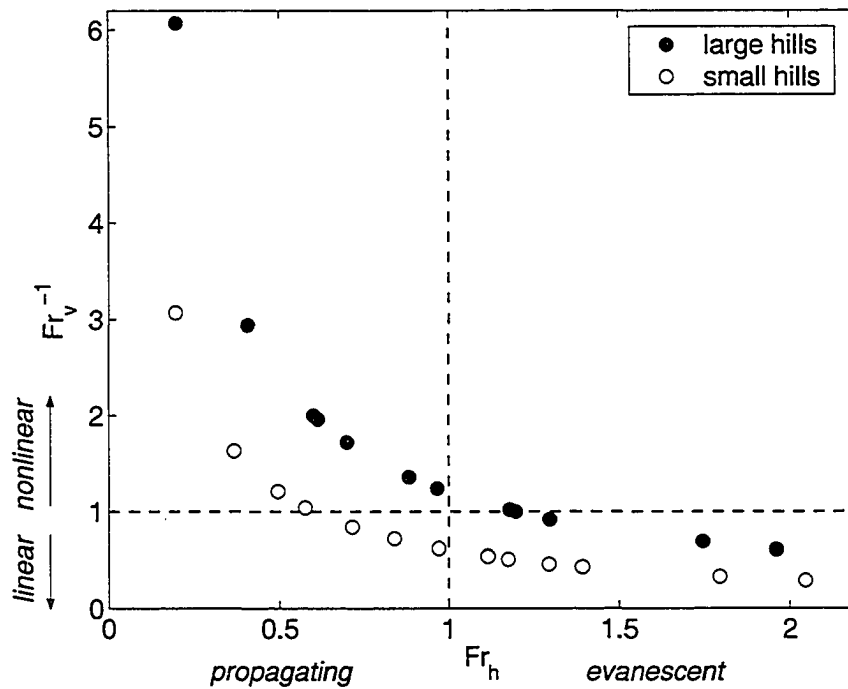
Figure 3.1: Summary of experiments in terms of horizontal and inverse vertical Froude numbers. Linear and nonlinear regimes are identified using Fr_v^{-1}, while propagating and evanescent waves are identified using Fr_h. The open circles are for the small-amplitude hills with relative amplitude $(H/2)/\lambda = 0.047$ or $Hk \simeq 0.6$, and the closed circles are for the large-amplitude hills with $(H/2)/\lambda = 0.095$ or $Hk \simeq 1.2$.

24

are taken at a horizontal location corresponding to the initial position of the first hill crest, thus capturing the movement of the remaining three hill crests through this location. The range of contours for the large-hill images is twice that for the small-hill images, thus highlighting the amplitude relative to the topographic height.

Figure 3.2a,b presents cases where $Fr_h < 1$ while Figure 3.2c,d presents cases where $Fr_h > 1$. For conceptual convenience in imagining flow over bottom topography, the images have been flipped vertically and the z-axis has been rescaled such that $z = 0$ corresponds to the bottom of the topography. The near-hill region of the vertical time series of the raw image is superimposed at the bottom of the frame. This is done to reveal flow structures in the valleys and in the lee of topography and so illustrate the relationships between the excitation mechanisms and the resulting wave fields. In any case, quantitative schlieren cannot be used to compute wave amplitudes in this region where the image of horizontal lines is often blurred by turbulence.

The regularity of the wave field for $Fr_h < 1$ is evident for both hills in Figure 3.2a,b. Comparing the horizontal distance between successive hilltops with the distance between successive crests or troughs, they are approximately the same. This is consistent with the expectation based on linear theory that the internal waves generated in these cases have frequencies that match the excitation frequencies. Two subtle, yet important, distinctions can be made between the images in Figure 3.2a,b. The first concerns waves generated directly over the hills, in which case the amplitude of the wave field relative to the hill height is slightly greater in the small hill experiment. The second concerns the waves in the lee of the last hills, in which case a rather significant increase in amplitude is evident in the large hill experiment and only a slight increase in the small hill experiment. This increase is associated with the flow structure in the lee of the last hill (see Figure 3.2b) and is described in the

25
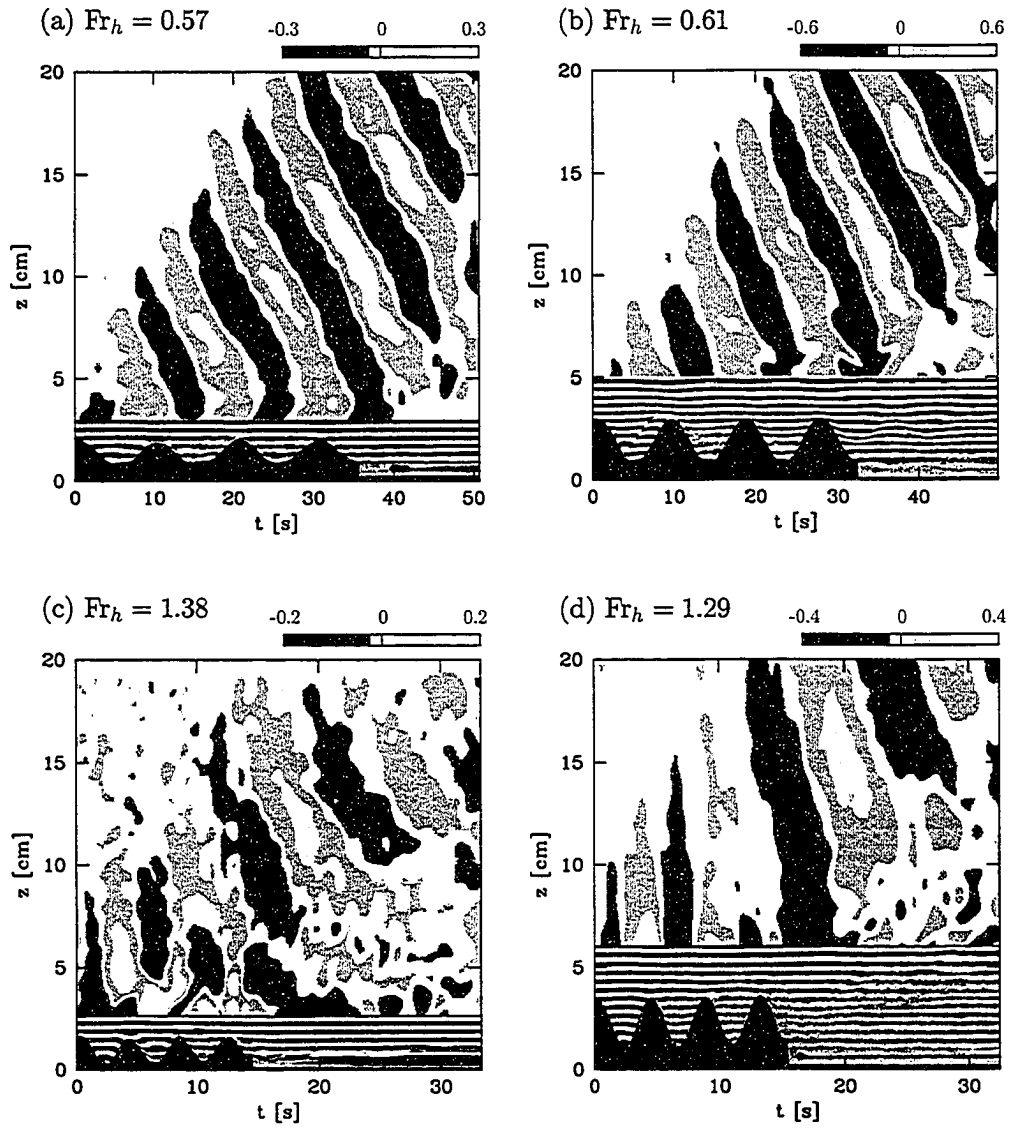
Figure 3.2: Vertical time series of N_t^2 [s^{-3}] for the small- and large-amplitude hills for the cases of $Fr_h < 1$ (a,b) and $Fr_h > 1$ (c,d). Vertical time series of the near-hill region of the raw images are superimposed to help visualize the correlation of the vertically-propagating internal waves relative to the topography and to observe boundary layer separation and boundary-trapped lee waves (see Section 3.2.2).

26

next subsection.

In Figure 3.2c,d, corresponding to supercritical wave excitation ($Fr_h > 1$), propagating internal waves are not generated directly over the topography but are observed, however, in the lee. These lee waves have longer periods, despite their rapid period of excitation. The generated wave frequencies, determined from the distance between successive crests or troughs in Figure 3.2c,d, are approximately equal, even though the hill heights, towing speeds, and relative amounts of turbulence are different. There is some evidence of high frequency, evanescent waves in the initial stages of the experiments. However, these motions decay before the hills pass and do not persist in the lee.

3.2.2 Boundary Layer Separation

In this subsection, we qualitatively examine the region near and in the lee of the hills in order to understand the generation of the previously presented wave fields. We select eight sample vertical time series of the near-hill region, which illustrate well the effects of increasing Fr_h and H.

Figure 3.3a-d compares images for $Fr_h < 1$. For the small hills, there is little distortion of the horizontal lines. However, for the large hills, there are significant distortions both between the hills and directly in their lee. In particular, in Figure 3.3b the flow over and between the hills ($t \approx 0 - 25\,\text{s}$) separates from the lee-side slope of the hills, forming stagnant patches of fluid between the hills and reducing the effective hill height. This is also apparent, although to a lesser extent, in Figure 3.3d and helps to explain the decreased relative wave amplitude observed in Figure 3.2b compared to 3.2a for $t \approx 0 - 25\,\text{s}$.

In the lee of the last hill ($t \approx 30 - 50\,\text{s}$ for Figure 3.3b and $t \approx 20 - 40\,\text{s}$ for 3.3d), the distortion of the lines reveals an undular shear layer, which begins where the boundary layer separates from the lee-side of the last hill.

27

(a) $\mathrm{Fr}_h = 0.37$, $\mathrm{Fr}_v^{-1} = 1.63$
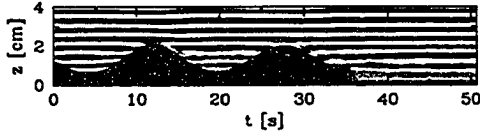
(b) $\mathrm{Fr}_h = 0.41$, $\mathrm{Fr}_v^{-1} = 2.94$
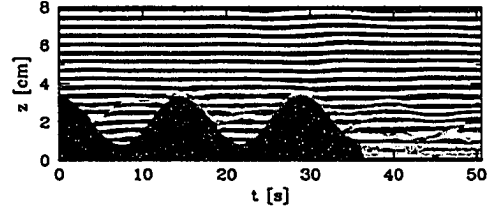
(c) $\mathrm{Fr}_h = 0.71$, $\mathrm{Fr}_v^{-1} = 0.84$
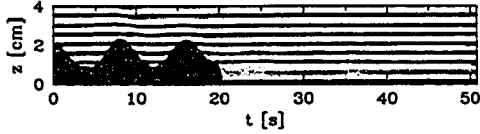
(d) $\mathrm{Fr}_h = 0.61$, $\mathrm{Fr}_v^{-1} = 1.96$
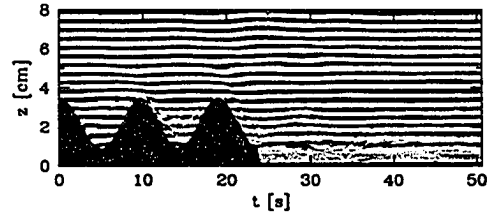
(e) $\mathrm{Fr}_h = 1.17$, $\mathrm{Fr}_v^{-1} = 0.51$
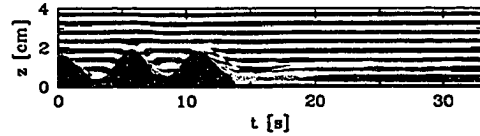
(f) $\mathrm{Fr}_h = 1.17$, $\mathrm{Fr}_v^{-1} = 1.02$
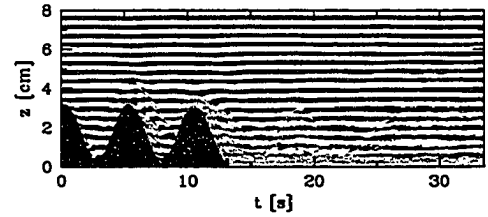
(g) $\mathrm{Fr}_h = 2.03$, $\mathrm{Fr}_v^{-1} = 0.30$
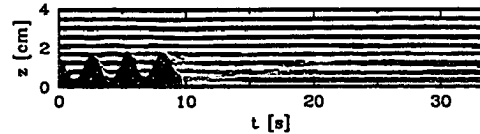
(h) $\mathrm{Fr}_h = 1.95$, $\mathrm{Fr}_v^{-1} = 0.64$
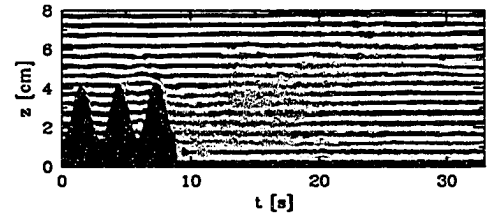
Figure 3.3: Sample vertical time series of the near-hill region, illustrating the distortion due to boundary-trapped lee waves and turbulence. The images on the right (b, d, f, and h) are those for the large-amplitude hills. Boundary-trapped lee waves are generated for a wide range of Fr_h. For large Fr_h, the region in the lee becomes turbulent, although still present is a well-defined boundary-trapped lee wave.

28

This boundary-trapped lee wave is similar to that observed downstream of a single "Witch of Agnesi" hill in three experiments by Baines and Hoinka (1985) (with parameter values $Fr_v^{-1} = 0.8$, 0.9, and 1.1 based on total hill height and, respectively, $Fr_h = 3.2$, 2.8, and 2.3 based on hill half-width), and downstream of a smooth step as observed in a range of experiments by Sutherland (2002).

A similar lee structure is observed at all Fr_h values for the large hills, yet only for select values for the small hills, particularly $Fr_h \gtrsim 1$. For example, a boundary-trapped lee wave is clearly distinguishable in Figure 3.3e but not in 3.3a,c.

Figure 3.3f,h illustrates the effect of increasing Fr_h on the lee structure of the large hills. In particular, as Fr_h increases, the flow in the lee becomes increasingly turbulent. Even so, there remains a coherent boundary-trapped lee wave separating the turbulent mixed regions from the remaining fluid above, the structure of which remains relatively constant.

For the small hills, turbulence is also generated, although to a much lesser extent (compare for example Figure 3.3g to 3.3h). As a result, the structure of the boundary-trapped lee wave is more difficult to identify. In all cases where boundary-trapped lee waves are formed, the wave is stationary with respect to the topography. The relationship between the boundary-trapped and resulting vertically-propagating lee waves is examined quantitatively in Section 3.3.2.

3.3 Quantitative Results

3.3.1 Power Spectra

Internal wave frequencies and wavenumbers are determined quantitatively from the N_t^2 fields using spectral methods. The choice of whether to use the vertical or horizontal time series depends on the types of wave features present. In particular, for the slower tow-speed experiments, the vertical time series are

29

preferred because they clearly distinguish between the waves generated over and in the lee of the topography, as seen in Figure 3.2a,b for example. Thus, windows can be carved from the original time series to isolate the different waves and then spectral methods can be applied separately to each window.

For example, for the time series given in Figure 3.2b, a window can be carved from $t = 0 - 25\,\mathrm{s}$ to isolate the topographically-generated waves and from $t = 25 - 50\,\mathrm{s}$ to isolate the waves generated in the lee. Figure 3.4 displays these two windows and the corresponding power spectra obtained by performing a two-dimensional Fourier transform on each of the windows. The location of the peak is used to measure the dominant frequency and vertical wavenumber. In this case, $(\omega, k_z) \approx (0.59, -0.56)$ for the waves over the hills and $(\omega, k_z) \approx (0.61, -0.66)$ for the waves in the lee. By averaging the peak values from time series at eight equally-spaced horizontal locations spanning approximately one hill wavelength, representative values are obtained. For this experiment, these are $\omega = 0.59 \pm 0.06\,\mathrm{s}^{-1}$ and $k_z = -0.59 \pm 0.14\,\mathrm{cm}^{-1}$ for the waves over the hills and $\omega = 0.62 \pm 0.06\,\mathrm{s}^{-1}$ and $k_z = -0.66 \pm 0.14\,\mathrm{cm}^{-1}$ for the waves in the lee, where the uncertainties are set by the resolution of the images.

For faster tow-speed experiments, where large-scale waves are generated in the lee, horizontal time series are preferred. This is because, in many cases, the vertical extent of the waves exceeds the vertical field-of-view and thus, the measurements of k_x are more reliable than those of k_z. Horizontal time series also have the advantage of capturing the movement of waves generated at the same time. Figure 3.5 shows a horizontal time series for the experiment of Figure 3.2d, along with its power spectrum. The horizontal time series is taken at a vertical location 15 cm below the peak of the topography. Again, by averaging the peak values of eight equally-spaced slices spanning approximately 8 cm, we obtain characteristic values, $k_x = 0.20 \pm 0.10\,\mathrm{cm}^{-1}$ and $\omega = 0.55 \pm 0.09\,\mathrm{s}^{-1}$.

30

(a) N_t^2 field - over hills

(b) Power Spectrum

(c) N_t^2 field - lee of hills

(d) Power Spectrum
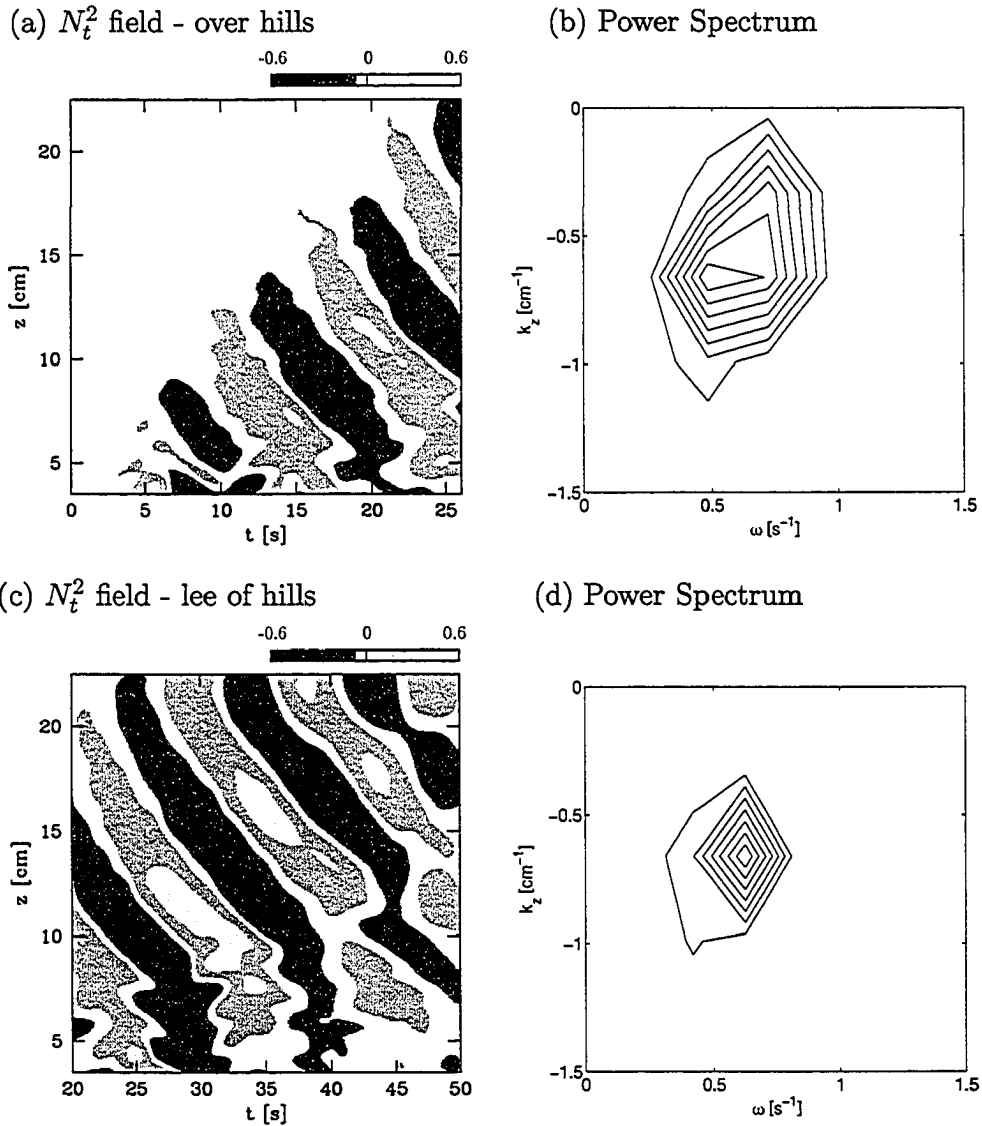
Figure 3.4: Select windows of the vertical time series of N_t^2 [s^{-3}] for the experiment shown in Figure 3.2b. The window in (a) isolates waves generated directly over the hills, whereas (c) isolates those generated in the lee. In (b) and (d) are the frequency and vertical wavenumber co-spectra determined from the images in (a) and (c) respectively.

31

(a) N_t^2 field   (b) Power Spectrum

(c) Power in k_x (d) Power in ω
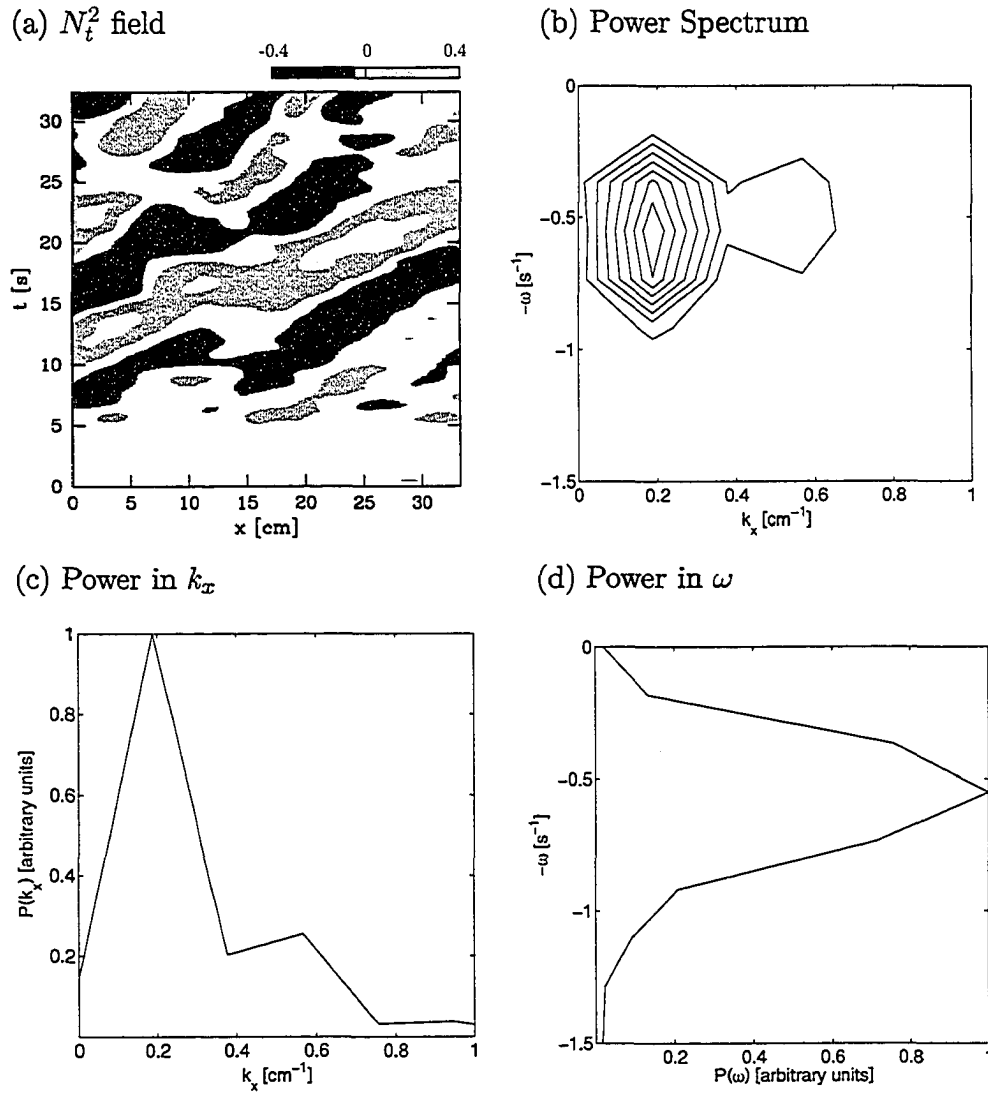
Figure 3.5: The frequency and vertical wavenumber spectra and co-spectrum for the experiment shown in Figure 3.2d. In (a) is the horizontal time series of N_t^2 taken at a vertical location 15 cm below the peak of the hills. In (b) is the power co-spectrum determined from (a). The $k_x - \omega$ spectrum is averaged over all ω values, resulting in the k_x-profile given in (c). Similarly, the ω-profile obtained by averaging over all k_x values is given in (d).

32

After having determined ω and one of either k_x or k_z, the other wavenumber component can be estimated using the dispersion relation (A.19).

In both Flynn and Sutherland (2004) and Dohan and Sutherland (2003), the estimates of ω and k_x (or k_z) are obtained by further averaging the co-spectrum over all k_x (or k_z) to determine ω and over all ω to determine k_x (or k_z). We found that the values obtained using this method were within the range of uncertainty of those determined from the peaks of the power spectrum. For example, Figure 3.5c,d gives the averaged k_x and ω profiles determined from the power spectrum in Figure 3.5b. The location of the peaks of these profiles are in agreement with the location of the peak of the power spectrum, as expected. Thus, the results presented in this report are those obtained from the average peak location of the power spectrum.

3.3.2 Wave Frequencies

Using the methods of the previous subsection, internal wave frequencies are determined for all experiments. The results are summarized in Figure 3.6, which plots the relative internal wave frequency, ω/N, as a function of the relative excitation frequency, $\omega_{exc}/N = \mathrm{Fr}_h$. Solid and open markers distinguish between waves generated directly over the hills and those generated in the lee, respectively. A vertical line clearly distinguishes two regimes, the first of which is termed the "propagation regime" in which $\mathrm{Fr}_h < 1$. In this regime, we see that the observed frequency of the propagating waves generated directly over the hills agrees well with the excitation frequency for sufficiently small Fr_h, but with significant departures occurring for $0.7 < \mathrm{Fr}_h < 1$. Thus, the linear theory prediction is valid for $\mathrm{Fr}_h \lesssim 0.7$ even though Fr_v^{-1} is of order unity (see Figure 3.1). Hence, the forcing mechanism is nonlinear. This result holds both for the small- and large-amplitude hills. In this regime we also notice that the frequency of the waves generated in the lee of the large-amplitude hills matches

33
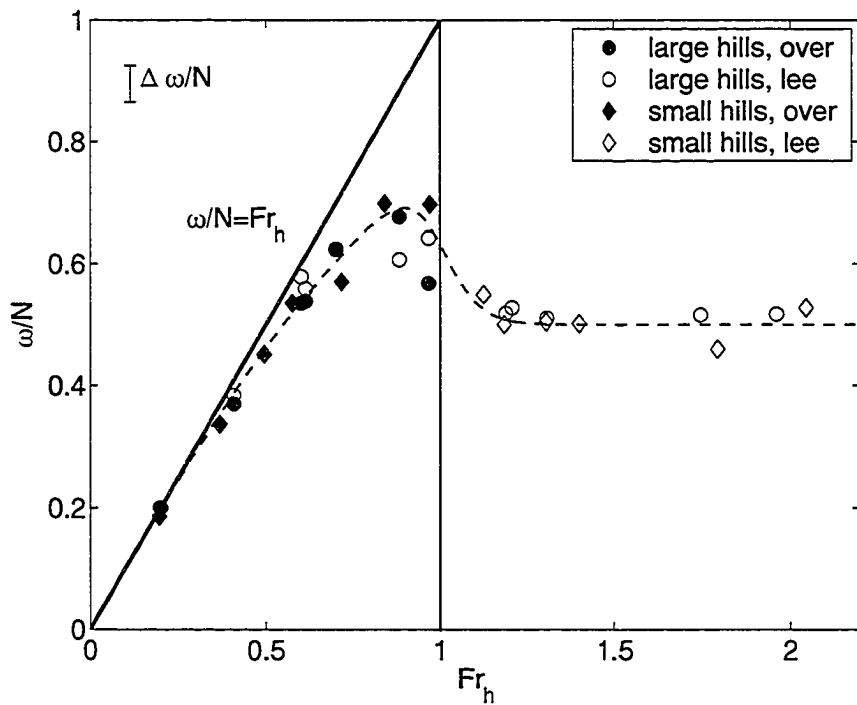
Figure 3.6: Plot of measured relative internal wave frequency, ω/N, as a function of relative excitation frequency, $\omega_{exc}/N \equiv \mathrm{Fr}_h$. The line $\omega/N = \mathrm{Fr}_h$ is plotted to compare the experimental measurements with those predicted by linear theory. The dashed line is an empirical fit to the data.

34

that of the topographically-generated waves, again with significant departure for $0.7 < \mathrm{Fr}_h < 1$.

In the "evanescent" regime for which $\mathrm{Fr}_h > 1$, propagating waves are no longer generated over the hills but nonetheless occur immediately in the lee of the range. The towing speed is so fast that the fluid does not traverse the valleys but rather flows over them, resembling flow over a single "envelope" of hills or a plateau. This "plateau effect" has been used to describe flow over the coastal terrain of the Western United States and Canada (Braun et al., 1999). To leading order, the waves in the lee are generated as a result of flow down the trailing slope of the plateau and in this sense resemble the waves generated by flow over a smooth step as examined by Sutherland (2002). As in that study, here we find the wave frequencies are an approximately constant fraction of the buoyancy frequency, N. In particular, $\omega/N \approx 0.51 \pm 0.02$. One might anticipate the ratio ω/N should be constant: if the horizontal length-scale, L, associated with the generation can be neglected, then the frequency must be determined by N^{-1}, not L/U. It is nonetheless remarkable that the frequency remains constant in the presence of vigorous turbulence.

As in Sutherland (2002), here we hypothesize that the waves are generated further downstream not only as a consequence of flow over the trailing slope of the envelope topography, but also through coupling with boundary-trapped lee waves. If the propagating and boundary-trapped waves are indeed coupled, we might expect their frequencies to match.

Using vertical time series images, the frequency of a boundary-trapped lee wave, ω_{lee}, is determined approximately by measuring the time between the crest of the last hill and the first crest of the hump-shaped disturbance, as shown, for example, in Figure 3.3f, which gives $T_{lee} \approx 8\,s$. Figure 3.7 compares the vertically-propagating and boundary-trapped lee wave frequencies for all applicable experiments. When $\mathrm{Fr}_h < 1$, the frequencies match well.

35
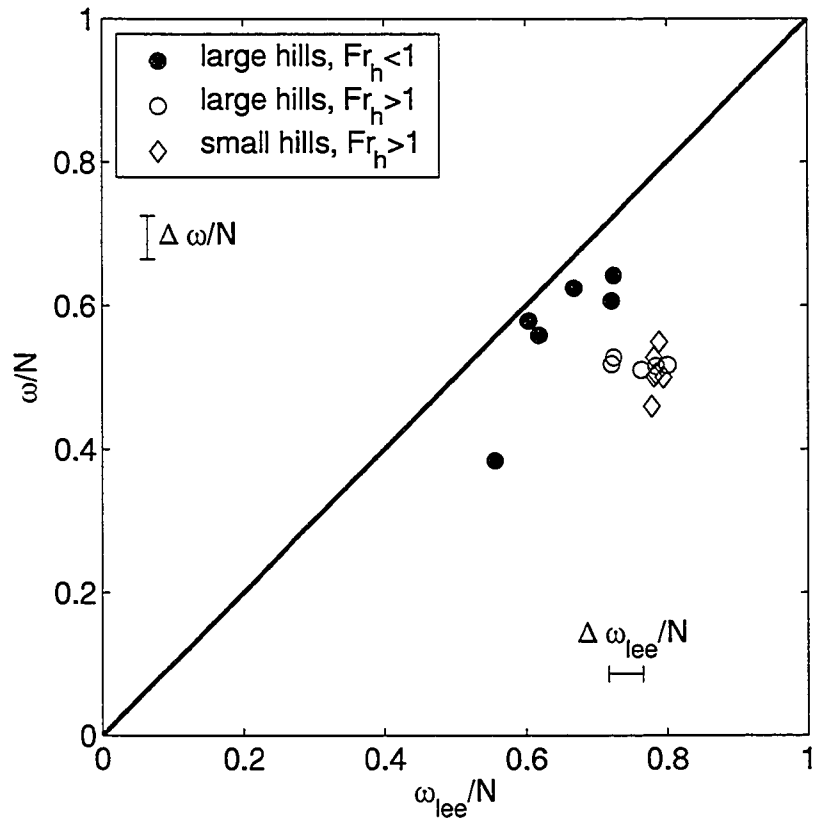
Figure 3.7: Comparison of propagating and boundary-trapped lee wave frequencies for experiments in which lee waves are clearly present.

36

In such cases, $\omega_{lee} \approx \omega \approx \omega_{exc}$. Like the propagating wave frequency, when $Fr_h > 1$ the boundary-trapped lee wave frequency is approximately constant but generally higher than ω/N. This is consistent with the study by Sutherland (2002), which found similar relationships between the propagating and boundary-trapped lee wave frequencies generated by a step-shaped topography.

As a way of providing a convenient summary of our experimental results, we have fit an empirical formula to the frequency data of Figure 3.6. The formula is of the form

$$f \approx wf_1 + (1 - w)f_2, \tag{3.1}$$

in which f_1 and f_2 describe the behaviour in the subcritical and supercritical regimes, respectively, and w is a weighting function. Explicitly, the empirical fit to the observed wave frequencies is

$$\omega/N = w[\tanh(Fr_h)] + (1 - w)[0.5], \tag{3.2}$$

in which the weighting function is given by

$$w(Fr_h) = 0.5(1 - \tanh[10(Fr_h - 1)]). \tag{3.3}$$

The graph of this function is given as a dashed line in Figure 3.6. The empirical fit to the data is very good, well within the uncertainty of the measurements.

3.3.3 Wave Amplitudes

One of the major advantages of using the synthetic schlieren technique is that it enables one to measure the internal wave amplitudes, according to the method described in Section 2.4. Figure 3.8 plots the relative internal wave amplitudes, $2A_\xi/H$, as a function of the horizontal Froude number, Fr_h. As in Figure 3.6, a vertical line divides the plot into two regimes and a thick horizontal line

37
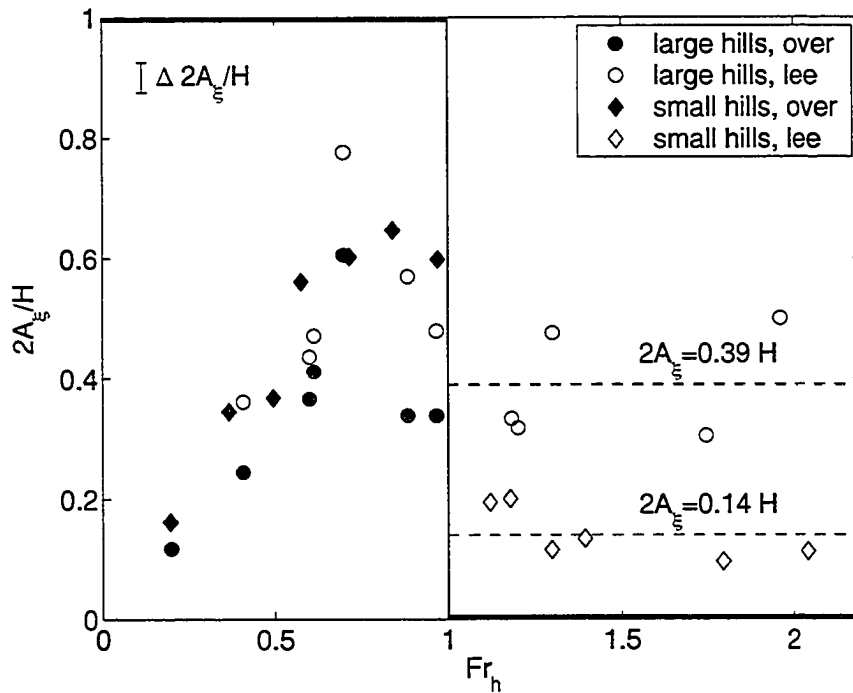
Figure 3.8: Plot of normalized internal wave amplitude, $2A_\xi/H$, as a function of Fr_h. The thick horizontal lines give the amplitude predicted by linear topographic forcing. The dashed lines give the average amplitude values for each hill height for $\mathrm{Fr}_h > 1$.

38

gives the linear theory prediction. Although linear theory predicts that the amplitudes of the waves generated over the hills should equal the hill amplitude for $Fr_h < 1$, this is clearly not the case. The wave amplitudes are significantly smaller, even for those generated over the small hills and especially for those generated over the large hills. This is an indication that nonlinear processes are important even for relatively smooth topography with $H/L = 0.1$.

We saw earlier (Figure 3.3b,d) for cases of $Fr_h < 1$ and $H/L = 0.2$ that fluid separated from the lee-side slopes of each hill and formed patches of trapped fluid in the valleys. This reduced the effective hill height. The important parameter that determines such separation is $Fr_v^{-1} = NH/U$. This parameter increases with increasing H or decreasing U, both of which contribute to generating adverse pressure gradients enabling boundary layer separation.

In our experiments (with the exception of one anomaly) the experiments with $Fr_v^{-1} > 1$ and thus, $Fr_h < 1$ according to Figure 3.1, generated waves over the hills having the smallest amplitudes, $2A_\xi \lesssim 0.4H$. It is in these cases that the nonlinear process of boundary layer separation dominates and significantly reduces the effective hill height. The majority of these experiments are for the large hills where we would expect nonlinear effects to be greater.

Figure 3.9 presents vertical time series of the near-hill region for the experiments with the highest Fr_v^{-1} values ($Fr_v^{-1} \gtrsim 3$). In these cases, the effects of boundary layer separation and flow blocking are most extreme and the resulting wave amplitudes are lowest. Recall from Section 2.2 that the reverse background flow was also most significant for $Fr_v^{-1} \gtrsim 3$ and thus, the reduced net flow speed likely contributes to increased blocking effects. Comparing Figure 3.9a to 3.9b, increasing H acts to increase the height of the blocked layer, while maintaining a relatively constant effective hill height as far as wave generation is concerned. This is consistent with the constancy of H_{eff} found in numerical simulations by Welch et al. (2001). In experiments with larger

39

(a) $\mathrm{Fr}_v^{-1} = 3.07$, $\mathrm{Fr}_h = 0.19$

(b) $\mathrm{Fr}_v^{-1} = 6.06$, $\mathrm{Fr}_h = 0.20$

(c) $\mathrm{Fr}_v^{-1} = 2.94$, $\mathrm{Fr}_h = 0.41$
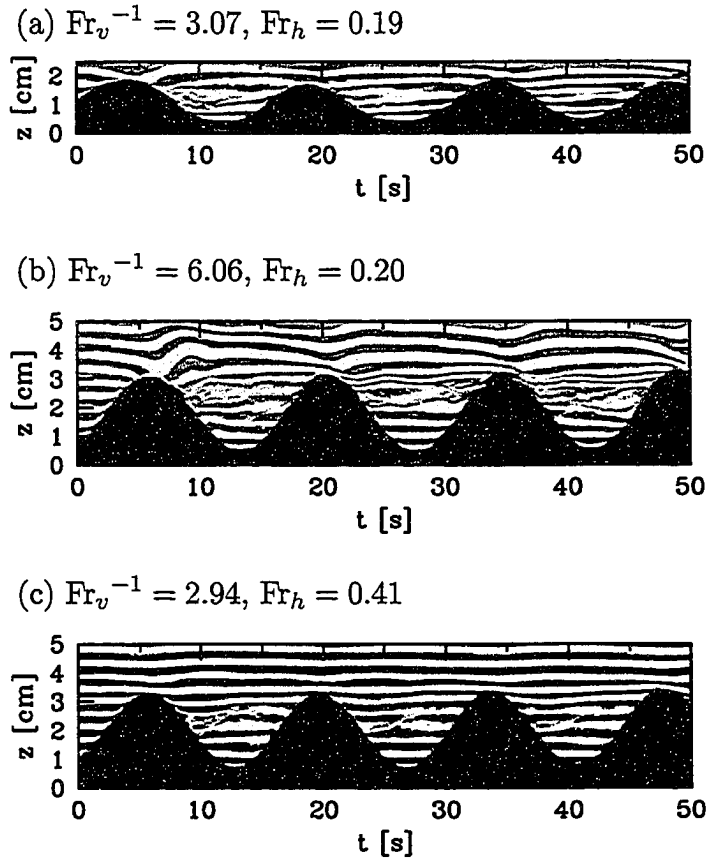
Figure 3.9: Vertical time series images of the near-hill region for experiments with large Fr_v^{-1}. The effects of flow separation and consequent trapping of fluid in the valleys are evident in all cases. The height of the blocked layer increases with increasing H (compare (a) with (b)) and decreases with increasing U (compare (b) with (c)).

40

towing speeds and thus smaller Fr_v^{-1} (Figure 3.9c), separation still occurs but further downstream the lee slope compared with that in 3.9b. The experiments show that for fixed Fr_h, Fr_v^{-1} limits the effective hill height and thus, the amplitudes of waves generated over the hills.

Apart from the waves generated over the hills, Figure 3.8 also gives the amplitudes of the waves generated in the lee of the hills, which result from flow over the lee-side slope of the last hill and the boundary-trapped lee wave as discussed earlier. For $Fr_h < 1$, only those waves generated in the lee of the large hills are included. This is because the small hills failed to generate well-defined boundary-trapped lee waves and as a result, the amplitude of the wave field increased only slightly in the lee. From Figure 3.8, the amplitudes of the waves generated in the lee of the large hills are greater than those generated over the hills, varying from $10 - 40\%$ greater. This is expected because the waves are generated in part by flow over the larger-amplitude boundary-trapped lee waves.

In the supercritical regime ($Fr_h > 1$), the propagating lee wave amplitudes remain large for the large-amplitude hills ($2A_\xi/H \approx 0.39 \pm 0.11$) but decrease significantly for the small-amplitude hills ($2A_\xi/H \approx 0.14 \pm 0.07$). These average values are presented as dashed lines in Figure 3.8. Because the propagating and boundary-trapped lee wave frequencies do not match in this case (Figure 3.7), we conclude that the waves are generated by a combination of flow over envelope topography and the boundary-trapped lee wave. We know the boundary-trapped lee wave continues to play a significant role because the propagating wave amplitudes are larger for the large-amplitude hills and the corresponding boundary-trapped lee waves also have significantly larger amplitudes (compare, for example, Figure 3.3g and 3.3h).

3.3.4 Analysis

As mentioned in Chapter 1, the momentum flux is an important and particularly useful quantity in terms of predicting and understanding atmospheric winds. The vertical flux of horizontal momentum, $\mathcal{F}_{uw}$, can be determined using the measured amplitudes and frequencies according to (A.22). The momentum fluxes for a range of experiments are plotted as a function of the horizontal Froude number in Figure 3.10. Here, the measured fluxes, $\mathcal{F}_{meas}$, are normalized by the maximum flux predicted by linear theory, $\mathcal{F}_{max} = \frac{1}{4}\rho_0 N^2 (\frac{H}{2})^2$. A curve representing the momentum flux that would result if $A_\xi = H/2$ is provided for reference. The general trends are similar to those of Figure 3.8. Note that the measured values are consistently lower than the theoretical values for $\mathrm{Fr}_h < 1$. Due to their larger amplitudes for $\mathrm{Fr}_h > 1$, the waves generated from the large-amplitude hills are able to transport momentum where linear theory predicts there to be no waves.

As a way of summarizing the amplitude and frequency results presented thus far, we present them in the form of a stability diagram in Figure 3.11 (Flynn and Sutherland, 2004; Dohan and Sutherland, 2003). This figure includes the critical amplitudes for two types of internal wave instabilities, namely overturning (denoted "OT") and self-acceleration (denoted "SA"). Overturning refers to the instability that occurs when dense fluid overlies less dense fluid. The critical relative amplitude for this instability is given by:

$$A_{OT} = \frac{1}{2\pi} \cot \Theta. \qquad (3.4)$$

Self-acceleration occurs when the wave-induced mean flow approaches the horizontal group velocity of the waves. The effect is to alter wave propagation and particularly, increase wave amplitude. When the wave-induced mean flow exceeds the horizontal group velocity, then the waves may become unstable and break. The critical relative amplitude for this instability is given by (Suther-
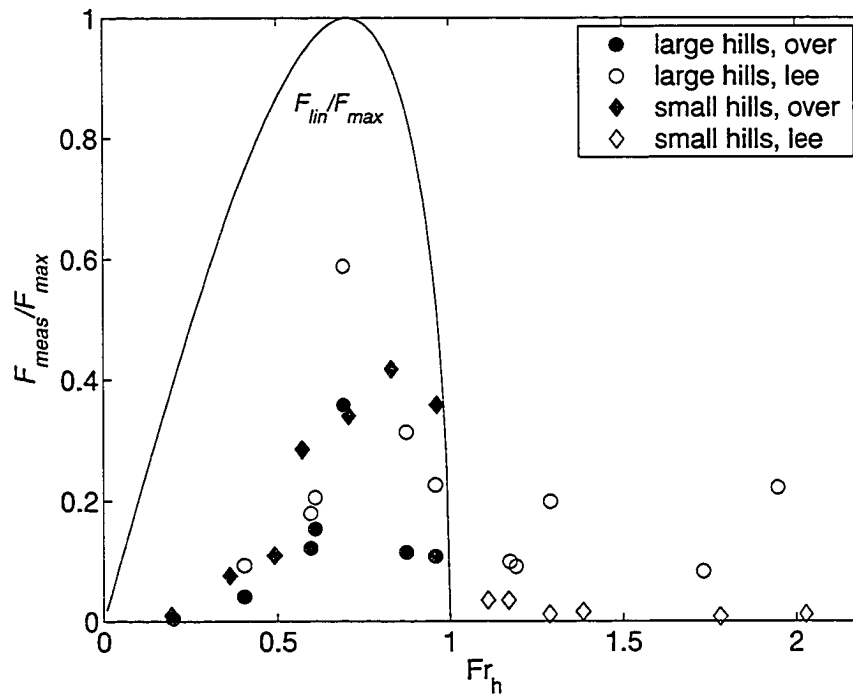
Figure 3.10: Plot of normalized vertical flux of horizontal momentum, $\mathcal{F}_{meas}/\mathcal{F}_{max}$, as a function of Fr_h. The measured flux, $\mathcal{F}_{meas}$, is normalized by a characteristic value of linear internal wave theory, $\mathcal{F}_{max} = \frac{1}{4}\rho_0 N^2(\frac{H}{2})^2$. A curve representing the flux predicted by linear theory is plotted for reference.

43
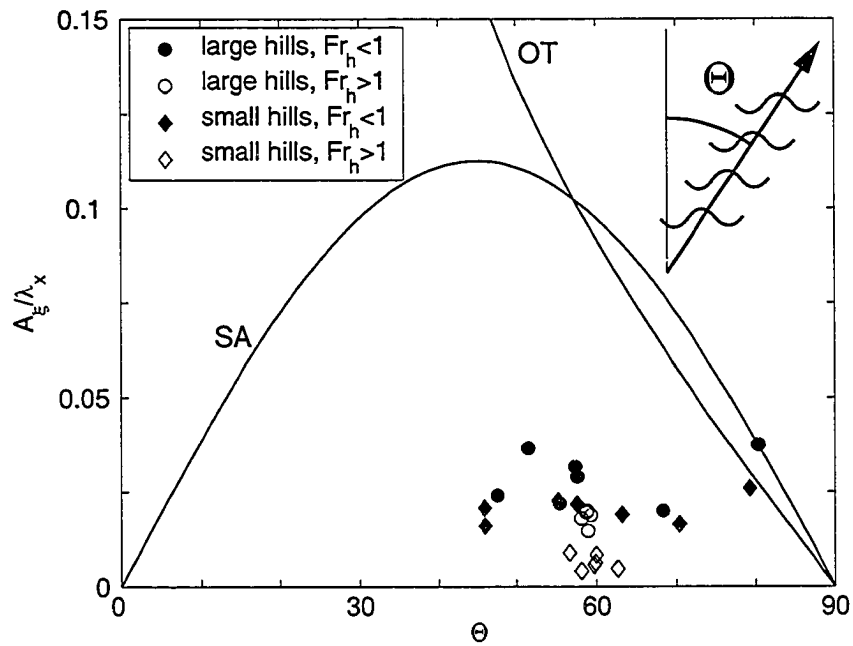
Figure 3.11: Plot of relative wave amplitude, A_ξ / λ_x, as a function of the angle of wave propagation to the vertical, Θ. The curve denoted "SA" is the critical relative amplitude at which the waves should become unstable by self-acceleration. The curve denoted "OT" is the relative amplitude at which the waves should overturn.

44

land, 2001)

$$A_{SA} = \frac{1}{2\pi\sqrt{2}} \sin 2\Theta. \tag{3.5}$$

There are two main observations to be made from Figure 3.11. First of all, with the exception of the open triangles, the waves are relatively large in the sense that the wave amplitudes are 2 - 4% of the horizontal wavelengths and 20 - 40% of the breaking amplitudes. Secondly, for the case of $Fr_h > 1$, the angles of propagation to the vertical lie within a very narrow range about $\Theta \approx 58^\circ$, corresponding to the narrow frequency range. The importance of these findings will be discussed together with those of the rough topography in Section 4.3.3.

3.4 Comparison with Long's Model

In this section, we compare the theoretical results of Long's model (Long, 1953) with our experiments. Long's model is an equation for the steady stream-function perturbed due to flow over topography of arbitrary amplitude (see Appendix B). As such, it is an improvement over linear theory which, strictly speaking, is applicable only for wave generation from infinitesimally-small amplitude hills. Even so, we do not expect excellent agreement between Long's model and our experiments because the model assumes the flow over topography is steady, inviscid, and free-slip, and so does not take into account the initial transient development of the waves, boundary layer separation, trapping of dense fluid in valleys, and the generation of turbulence.

Despite these limiting assumptions, the model has been used, for example, as an initial condition for numerical simulations examining upper-level internal wave breaking in the atmosphere above isolated topography and the consequent generation of downslope winds (Laprise and Peltier, 1989; Scinocca and Peltier, 1989). Although these simulations assumed inviscid flow, and hence

45

neglected boundary layer separation, this assumption is not necessarily valid for topography having steep slopes or topography consisting of two or more hills whereby dense fluid can be trapped in the valleys. Even in the case where the flow is relatively fast, and Fr_v^{-1} small, we have seen that boundary layer separation results in the shedding of coherent turbulent structures in the lee of topography, which alters wave generation.

The purpose of this section is to compare the predictions of Long's model against our laboratory experiments and thereby further examine the role of boundary layer separation in these moderately-large Reynolds number flows.

The solutions of Long's model under the conditions of the two small-amplitude hill experiments shown in Figure 3.2a,c are presented in Figure 3.12. Figure 3.12a is computed using the solution method for integral equations of the first-kind, which gives good convergence for this small value of Fr_h. The method for second-kind integral equations is used to compute the solutions shown in Figure 3.12b, in which the waves are significantly non-hydrostatic. Both are the steady-state solutions for flow over 4 sinusoidal hills and, for ease of comparison, the results are presented as vertical time series rather than spatial snapshots. (See Appendix B for further details regarding solution methods.)

Qualitatively, Long's model captures the features we observe in these two experiments. In the case with $Fr_h < 1$ (Figure 3.12a), vertically propagating waves are generated with upstream phase tilt and waves in the lee have slightly larger amplitude than those over the hills. In the case with $Fr_h > 1$ (Figure 3.12b), waves generated directly over the hills are evanescent but a transient burst of vertically-propagating waves appears in the lee of the last hill.

Although good qualitative agreement is found, Long's model predicts that the wave amplitude is significantly larger than observed in experiments. Note,

46
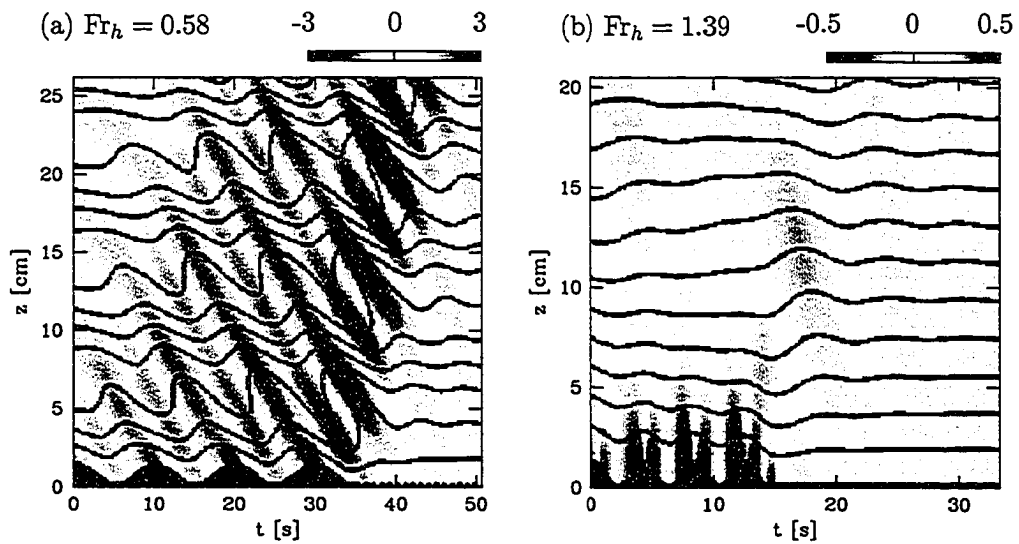
Figure 3.12: Long's model solution for (a) subcritical and (b) supercritical forcing corresponding to the experiments shown in Figure 3.2a and 3.2c respectively. The colour contours show values of N_t^2 [s^{-3}], though the ranges differ from those in Figure 3.2. The black lines are streamlines.

47

for example, that the range of the contours is 10 times larger in Figure 3.12a than in the corresponding plot in Figure 3.2a. Furthermore, the streamlines in Figure 3.12a are overturning, although overturning is not observed in the experiment. Likewise, though not shown here, Long's solution computed for the large-amplitude experiments shown in Figure 3.2b,d predicts the generation of waves of much larger amplitude than are actually observed. Also, waves are predicted to be overturning, though this is not what we find in experiments with the large-amplitude hills.

A simple linear theory calculation predicts that overturning above infinitely periodic sinusoidal hills with half peak-to-peak hill height, $H/2$, should occur if

$$\frac{H}{2} > \frac{\lambda}{2\pi} \frac{\mathrm{Fr}_h}{\sqrt{1 - \mathrm{Fr}_h^2}}. \tag{3.6}$$

For the experiment shown in Figure 3.2a, this overturning condition becomes $H/2 \gtrsim 0.11\lambda$. The small-amplitude hills in fact satisfy $H/2 = 0.047\lambda$, well below the overturning amplitude. There are two reasons why Long's model nonetheless predicts overturning. First, the hills have finite horizontal extent and the flow at the bottom boundary approaching from infinity is at the same vertical level as the bottom of the valleys, not the mid-depth between hill crests and valleys. Thus the flow is displaced by the peak-to-peak distance, not half that value. Second, nonlinear dispersive effects, such as self acceleration, act to increase the amplitude of the waves further so that they become overturning.

We might then expect to see overturning in the laboratory experiments and yet, we do not. One of the reasons is that Long's model does not permit boundary layer separation: the wave amplitude in the model is set directly by the hill height. Thus, the amplitude of waves generated in experiments is smaller because the flow over topography does not penetrate down to the bottom of the valleys between the hills but rather, fluid remains stagnant close

48

to the valley floors. Likewise, Long's model does not predict the generation of boundary-trapped lee waves and turbulence. Therefore, it does not account for the modification of propagating waves in the lee by these phenomena. Another reason we do not observe overturning in the experiments is because columnar motions are generated within the tank. Baines and Hoinka (1985) observed that columnar motions generated in the laboratory opposed the steepening of internal waves and thus, increased the critical value of NH/U above which overturning occurred compared to that predicted by Long's model.

3.5   Discussion

We have investigated internal wave generation over sinusoidal topography and compared our results with the predictions of linear theory and Long's model. For slow towing speeds ($Fr_h < 1$ and corresponding $Fr_v^{-1} > 1$), measured wave frequencies agree well with the excitation frequencies predicted by linear theory provided $Fr_h \lesssim 0.7$. However, linear theory significantly overestimates wave amplitudes, even for the small-amplitude hills with $H/L = 0.1$. This is also true for Long's model and can be explained by boundary layer separation, which acts to reduce the effective hill height. The generation of large-amplitude waves in the lee of the large-amplitude hills is also observed and couples with boundary-trapped lee waves. In particular, $\omega \approx \omega_{lee}$ in a range from 0.55 to $0.75N$. This is the same range observed by Sutherland (2002) for experiments using a large-amplitude step with $Fr_v^{-1} > 1$.

At supercritical towing speeds, vertically-propagating internal waves are observed in the lee of the topography. These waves, generated in part through excitation by envelope topography, also weakly couple with coherent turbulent structures in the lee, called boundary-trapped lee waves. Both the propagating and boundary-trapped lee waves are excited within a narrow range of frequencies, with $\omega < \omega_{lee}$ in general.

49

Chapter 4

Results: Rough Topography

4.1 Introduction

In this chapter we move away from the study of smooth sinusoidal hills and the corresponding theories that can be applied to such cases to study internal wave generation from more complex and rough topographies, namely rectangular and triangular hills. The hills are tall and steep with $H/L = 0.2$, the same value as for the large-amplitude sinusoidal hills (see Table 2.1). With such topographic shapes, the nonlinear effects of boundary layer separation and turbulence become even more important.

In this set of experiments, the model hills are towed at speeds ranging from $U = 0.83$ - 5.12 cm/s. The corresponding horizontal and inverse vertical Froude numbers range from $\mathrm{Fr}_h = 0.36$ - 2.10 and $\mathrm{Fr}_v^{-1} = 0.47$ - 3.42.

As in the case of the sinusoidal hills, propagating internal waves are generated both directly over the hills and in the lee via flow over envelope topography and boundary-trapped lee waves. In addition, smaller-scale waves are generated by a region of vigorous turbulence far in the lee of the topography. This is one of the key features that distinguishes stratified flow over rough topography from that over smooth topography. The qualitative nature of the wave fields is examined in the next section and related to the flow structure near the hills. Following this, quantitative measurements of fundamental

50

wave properties are presented and compared with those of the large-amplitude sinusoidal hills.

4.2 Qualitative Observations

4.2.1 Internal Wave Fields

We begin by presenting six sample vertical time series of N_t^2, three each for the rectangular and triangular hills, to illustrate the main characteristics of the wave fields as they depend on Fr_h. The images have been carefully selected to illustrate the three main types of internal waves that are generated from rough topography. As in Figure 3.2, the images have been flipped vertically and the vertical time series of the near-hill region of the raw image has been superimposed on the bottom of the image to help visualize the relationship between the flow and the wave generation mechanisms.

Figure 4.1a and 4.1b show two cases having $Fr_h < 1$. In both cases, waves are generated both directly over the hills and in the lee. For the rectangular hills, the wave intensity is significantly lower directly over the hills, a result of significant fluid trapping between the hills. At low Fr_h values, the corresponding Fr_v^{-1} values are very high and combined with the steep vertical slope, the fluid is forced to separate almost immediately from the hills forming large regions of trapped fluid. This is seen clearly in the raw image of the near-hill region shown in Figure 4.1a. Flow trapping is also present for the triangular hills in Figure 4.1b, where the fluid traverses only approximately half of the total hill height. For both hills, the depth of the trapped fluid decreases slightly with increasing Fr_h.

Also present in both Figures 4.1a and 4.1b is the outline of a boundary-trapped lee wave trailing the last hill. Qualitatively, the height of this structure is larger than the effective hill height and thus, helps to explain the increased
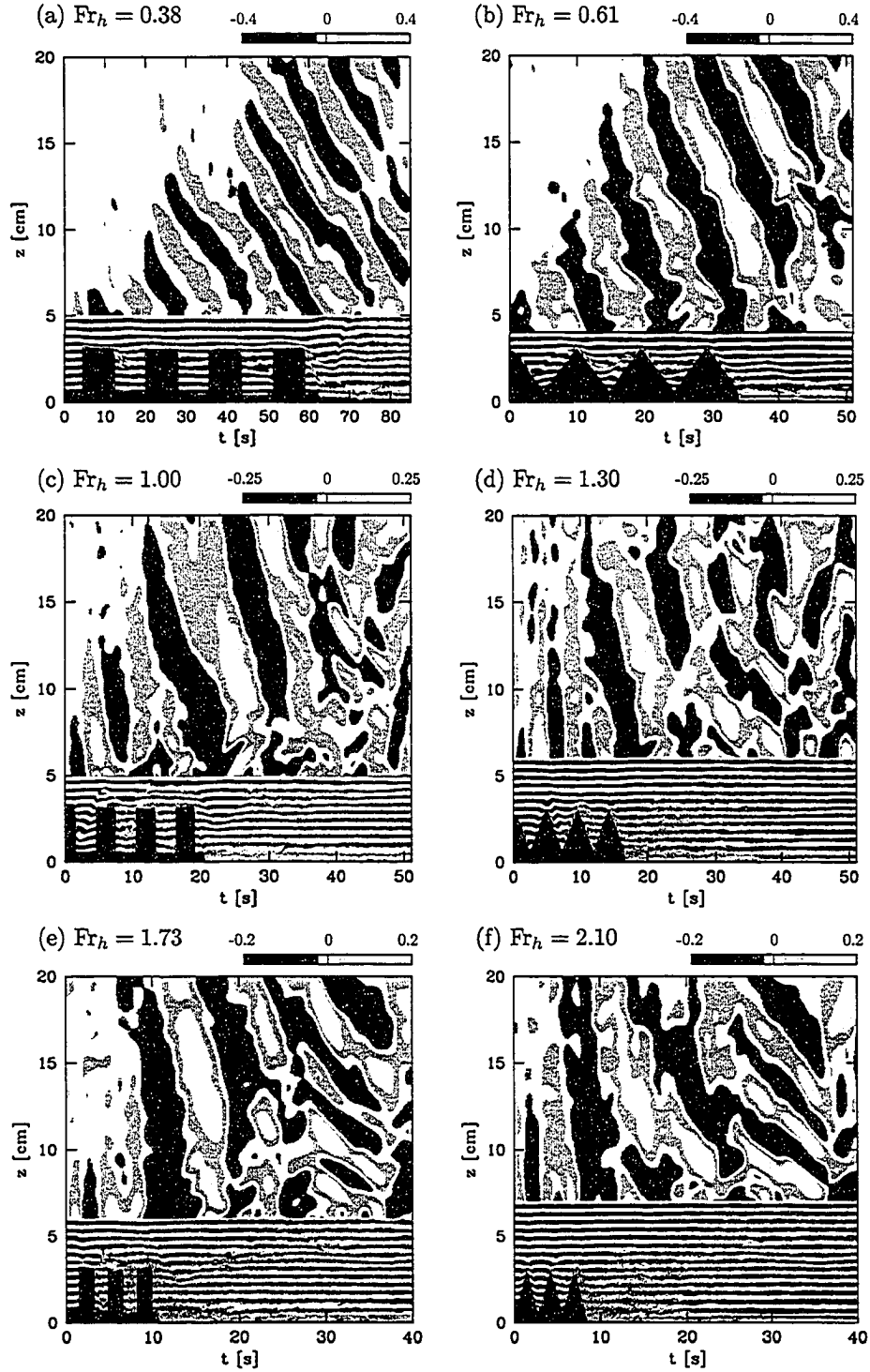
Figure 4.1: Vertical time series of N_t^2 [s^{-3}] for the rectangular and triangular hills for the cases of (a,b) Fr$_h$ < 1, (c,d) Fr$_h$ $\gtrsim$ 1, and (e,f) Fr$_h$ > 1. Vertical time series of the near-hill region of the raw images are superimposed to help visualize the vertically-propagating internal waves relative to the topography and boundary-trapped lee waves.

52

wave amplitudes observed in the lee.

Figure 4.1c presents a case where $Fr_h \approx 1$. Evanescent waves are generated over the hills ($t = 0 - 15\,\mathrm{s}$) followed by larger-scale vertically-propagating lee waves ($t = 15 - 30\,\mathrm{s}$), similar to those observed for the sinusoidal hills for $Fr_h > 1$ (see Figure 3.2d). Examining the near-hill region, we can clearly identify a boundary-trapped lee wave, whose first crest is well above the peak of the topography, located at $t \approx 17\,\mathrm{s}$, and second crest at $t \approx 28\,\mathrm{s}$. The distance between these two peaks roughly matches that between successive wave crests or troughs, suggesting that there may be a coupling between the two.

Still further in the lee, the boundary-trapped lee wave breaks up into a patch of turbulence, above which some smaller-scale wave structures begin to emerge ($t \approx 40\,\mathrm{s}$). These smaller-scale waves also appear for the triangular hills but only for $Fr_h > 1$. This is because flow over the triangular hills does not create as much turbulence as that over the rectangular hills for a given flow speed, U. Figure 4.1d shows a case where $Fr_h = 1.30$ for the triangular hills. The character of the wave field is similar to that of Figure 4.1c. Note that the lee wave amplitudes are slightly lower for the triangular hills, likely a consequence of the smaller amplitude of the boundary-trapped lee structure, as visualized in the raw hill image of Figure 4.1d compared to 4.1c.

Figures 4.1e and 4.1f present cases with very fast towing speeds, enabling the rapid development of a turbulent mixed region far in the lee of the topography. As in the previous images, boundary-trapped lee waves and corresponding propagating lee waves are clearly visible and the wave intensities are slightly higher for the rectangular hills. Of equal or greater importance, however, are the smaller-scale waves that radiate away from a turbulent mixed region ($t \approx 27 - 37\,\mathrm{s}$). The structure of the waves is remarkably uniform despite the random nature of turbulence.

53

In summary, through these six images, we clearly observe the complexity of wave generation from tall and rough topography. Waves are generated as a result of complex interactions between the flow and topography, including flow over boundary-trapped lee waves that form as a result of lee-side separation and vigorous turbulence that develops in the far lee of steep topography when the turbulent structures break apart. The characteristics of such waves, namely frequency and amplitude, are quantified and presented in the Section 4.3.

4.2.2   Near-Hill Flow Structure

In this section, several images of the near-hill region are presented for a wide range of Fr_h values with the purpose of emphasizing important features of the flow structure near and in the lee of the topography. These features will later help to explain the quantitative results of Sections 4.3.2 and 4.3.3.

Figure 4.2 presents six sample vertical time series of the near-hill region for experiments having $Fr_h < 1$. For the triangular hills, the fluid moves into and out of the valleys much like it does for the sinusoidal hills (compare Figure 4.2b,d,f with Figure 3.3b,d). For the rectangular hills, however, the effective shape of the hill is modified by the flow to resemble a smooth hill. In particular, the sharp edges are rounded and the valleys are filled in by either trapped stagnant fluid (Figure 4.2a,c) or by vortices, which subsequently break into patches of turbulence (Figure 4.2e).

Figure 4.3 presents eight sample images for experiments having $Fr_h > 1$. The most important feature of these images is a well-defined boundary-trapped lee wave trailing the last hill, as observed in Figure 3.3f,h for the sinusoidal hills. The difference between the flow structure over the different hills is the relative amount of turbulence created. As we saw in Figure 4.1c,e for the rectangular hills, the first crest of the boundary-trapped wave lies well above

54

(a) $Fr_h = 0.36$, $Fr_v^{-1} = 3.27$
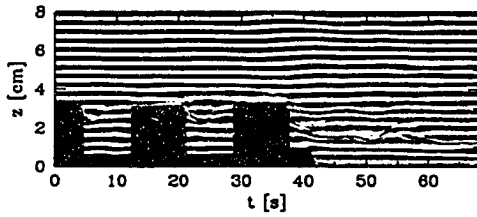
(b) $Fr_h = 0.39$, $Fr_v^{-1} = 3.06$
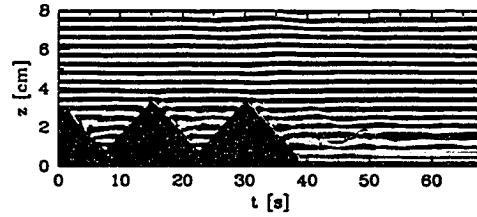
(c) $Fr_h = 0.53$, $Fr_v^{-1} = 2.27$
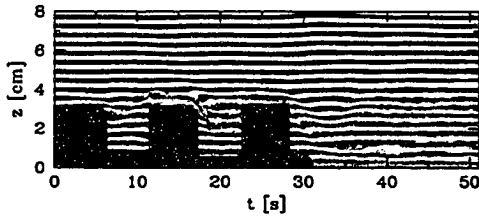
(d) $Fr_h = 0.61$, $Fr_v^{-1} = 1.96$
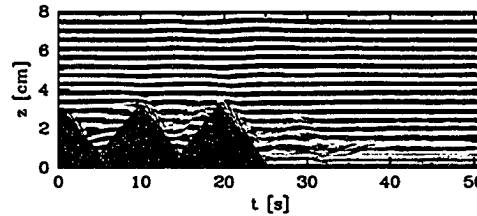
(e) $Fr_h = 0.76$, $Fr_v^{-1} = 1.57$
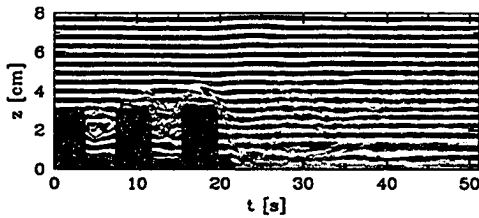
(f) $Fr_h = 0.73$, $Fr_v^{-1} = 1.62$
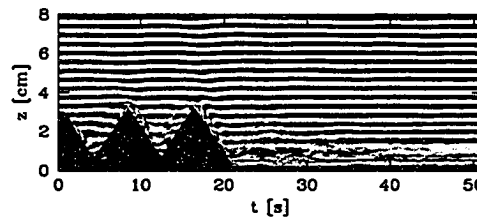
Figure 4.2: Sample vertical time series of the near-hill region for $Fr_h < 1$, illustrating the flow pattern above and in the lee of the hills. The sharp edges of the rectangular hills are smoothed by the interaction with the flow. Boundary-trapped lee waves are clearly present in all cases.

55
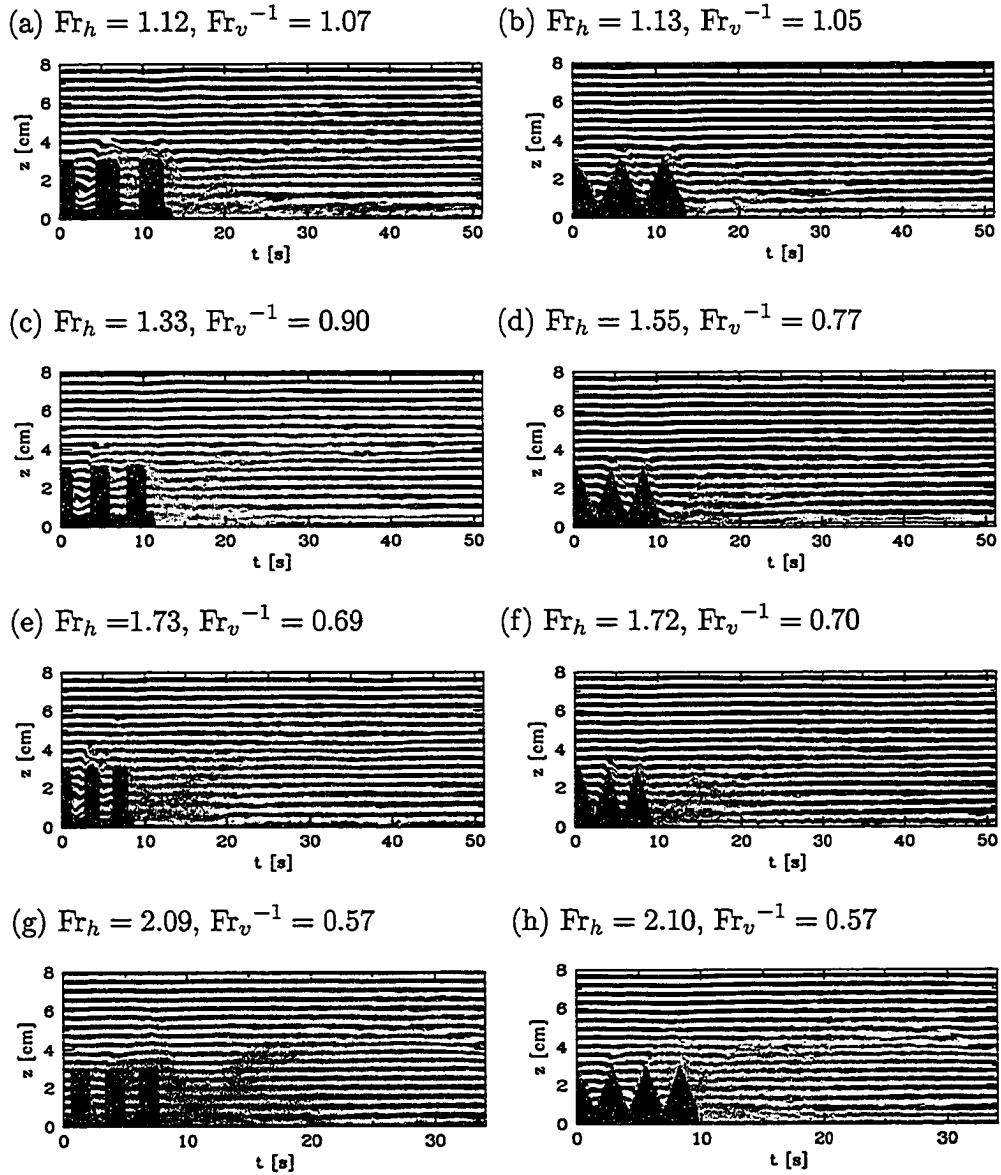
Figure 4.3: Sample vertical time series of the near-hill region for $Fr_h > 1$, illustrating the coherent nature of the boundary-trapped lee structure despite changes in topographic shape, towing speed, and consequent amounts of turbulence.

56

the peak of the topography and even more so as Fr_h is increased. Below the crest is a large patch of turbulence, which remains relatively stationary with respect to the topography. The turbulence acts to increase the effective height of the boundary-trapped lee wave. A second crest trails the first and is generally located at a lower vertical level. For the triangular hills, turbulence is created to a lesser extent and does not significantly increase the height of the lee structure for $Fr_h \lesssim 2$. Comparing Figure 4.3 to Figure 3.3f,h we see that the relative amount of turbulence generated over the sinusoidal hills lies somewhere between that of the rectangular and triangular hills.

4.3 Quantitative Results

4.3.1 Spectral Analysis

A procedure similar to that described in Section 3.3.1 is used to determine characteristic values of the frequency and wavenumbers for the different types of waves observed in these experiments. For experiments having $Fr_h < 1$, the method is identical, using vertical time series of N_t^2 and selecting windows to isolate the waves generated over and in the lee of the hills. For experiments having $Fr_h > 1$, the horizontal time series images are divided into windows to isolate the waves generated over the boundary-trapped lee waves and those generated by the turbulent mixed region. This step of selecting windows was not necessary for the sinusoidal experiments, in which smaller-scale waves were not observed.

Although turbulence itself is composed of many scales, the power spectra corresponding to the turbulence-generated waves exhibit, in most cases, a well-defined peak. Characteristic values for the wave frequency and horizontal wavenumber are obtained by taking the average peak value obtained from ten equally-spaced horizontal time series. Figure 4.4 presents six sample

57
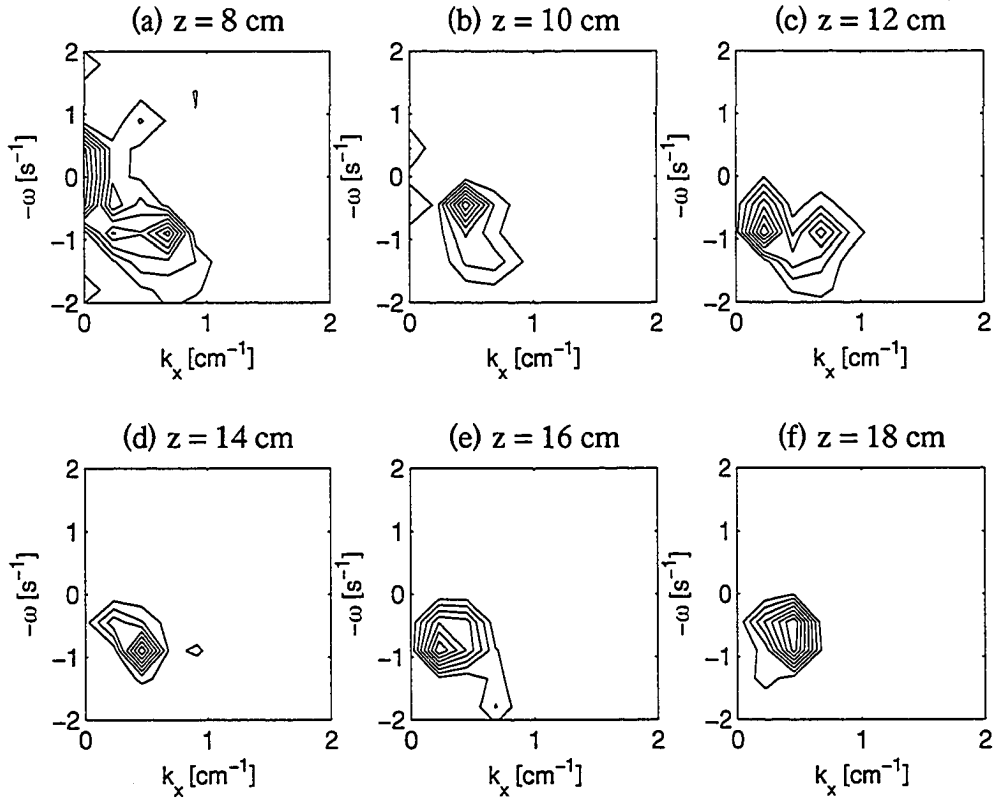
Figure 4.4: Sample power co-spectra corresponding to horizontal time series of N_t^2 taken at vertical locations from $z = 8 - 18$ cm for the experiment shown in Figure 4.1e. (Note that $z = 0$ cm corresponds to the bottom of the topography.) The peaks of the power spectra are used to obtain a characteristic value of frequency and horizontal wavenumber.

58

power spectra for the experiment shown in Figure 4.1e. For this experiment, the characteristic frequency and horizontal wavenumber of the turbulence-generated waves are $\omega = 0.76 \pm 0.14\,\mathrm{s}^{-1}$ and $k_x = 0.40 \pm 0.07\,\mathrm{cm}^{-1}$, where the uncertainty is determined from the standard deviation of the ten peak values.

4.3.2 Wave Frequencies

Figure 4.5 plots the relative frequencies of three types of propagating internal waves generated from the rectangular and triangular hills as a function of Fr_h. The chosen symbols correspond to the topographic shape (i.e. triangular symbol for the triangular hills and square symbol for the rectangular hills) and the shading to the type of wave (i.e. black markers for waves generated over the hills due to direct topographic forcing, open markers for waves generated in the lee, and grey markers for waves generated by the turbulent mixed region). A diagonal line representing the linear theory prediction for smooth hills is plotted for $Fr_h < 1$. As in the case of the sinusoidal hill experiments, the waves generated directly over the rough hills have frequencies that agree well with linear theory predictions for $Fr_h < 0.7$, despite the fact that the hills themselves are neither small-amplitude nor smooth. However, as we saw in Figure 4.2, the effective shape of the hills was smoothed by the flow. Thus, the mechanism by which the waves are generated in both cases is topographic forcing by relatively smooth topography and the results are what we might expect.

Also for $Fr_h < 0.7$, the frequencies of the propagating lee waves agree well with those generated over the topography. Again, this is consistent with the images in Figure 4.2, in which the boundary-trapped lee wave resembles a smooth extension of the topography. Beyond $Fr_h \approx 0.7$ the propagating lee wave frequencies lie within a relatively narrow range, in particular $\omega/N \approx 0.57 \pm 0.05$. Such a narrow frequency range was also observed in the

59

Figure 4.5: Plot of measured relative internal wave frequency, ω/N, as a function of horizontal Froude number, Fr_h. The line $\omega/N = Fr_h$ is plotted to compare the experimental measurements with those predicted by linear theory for smooth hills. Representative uncertainties, $\Delta\omega/N$, depend on the type of wave, i.e. "over,lee" for waves generated over or in the lee of the hills and "turb." for waves generated by the turbulent mixed region.

60

experiments using the large-amplitude sinusoidal hills, although with slightly smaller values ($\omega/N \approx 0.51 \pm 0.02$).

As in the sinusoidal hill experiments, the propagating lee waves are generated as a result of flow over both envelope topography and the undular structure trailing the last hill. Figure 4.6 compares the frequencies of the vertically-propagating and boundary-trapped lee waves. The data for the large-amplitude sinusoidal hills is included for comparison purposes (circular markers). For all hill shapes, there is a strong coupling for $Fr_h < 1$. In particular, the coupling is strongest for the rectangular data, both for $Fr_h < 1$ and $Fr_h > 1$. This is consistent with the constancy of the lee structure across all Fr_h for the rectangular hills (Figure 4.2b,d,f and 4.3b,d,f,h).

For $Fr_h > 1$ the coupling is weaker and there appears to be some shape dependence. In all cases, however, the data are clustered within a relatively narrow range of frequencies, with the boundary-trapped lee wave frequencies slightly higher than those of the propagating waves. The effect of flow over envelope topography, as introduced in Section 3.3.2, may act to decrease the propagating wave frequencies.

As a way of comparing the results thus far with those of the large-amplitude sinusoidal hills, Figure 4.7 plots the relative wave frequencies generated over and in the lee of the large-amplitude sinusoidal and rough hills. The results collapse onto a single curve in both circumstances.

Returning to Figure 4.5, in particular the regime where $Fr_h > 1$, we examine the waves generated by the turbulent mixed region far in the lee of the steep rectangular and triangular hills. Like the waves in the immediate lee, we find that these smaller-scale waves are also generated within a narrow frequency range, independent of the topographic shape. In particular, the average relative frequency of the combined data points is $\omega/N \approx 0.72 \pm 0.05$. Such a narrow frequency range was also observed in the mixing box exper-
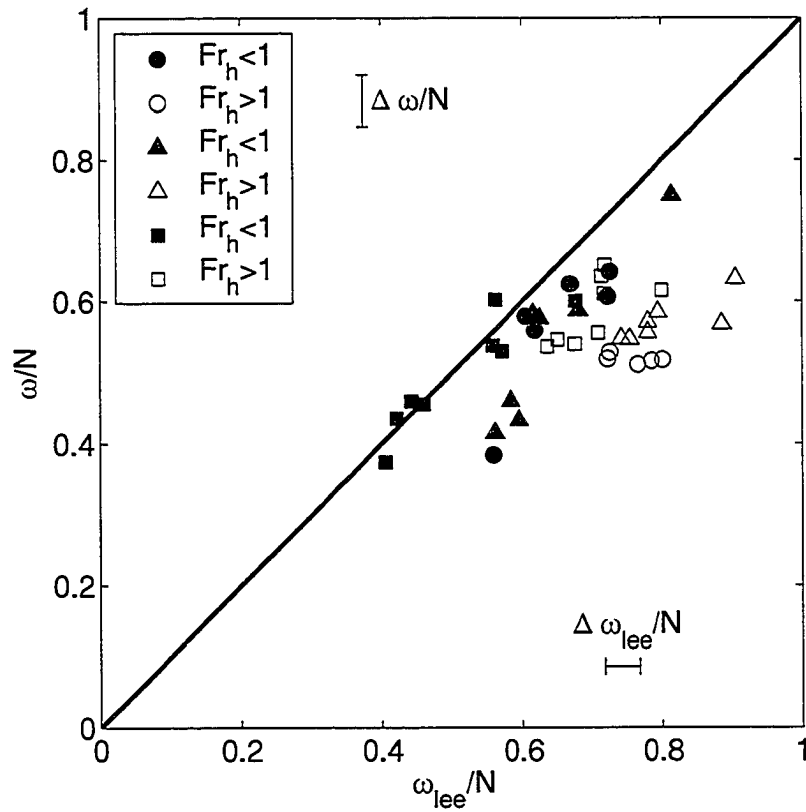
Figure 4.6: Comparison of vertically-propagating and boundary-trapped lee wave frequencies for experiments using the large-amplitude sinusoidal, triangular, and rectangular hills.
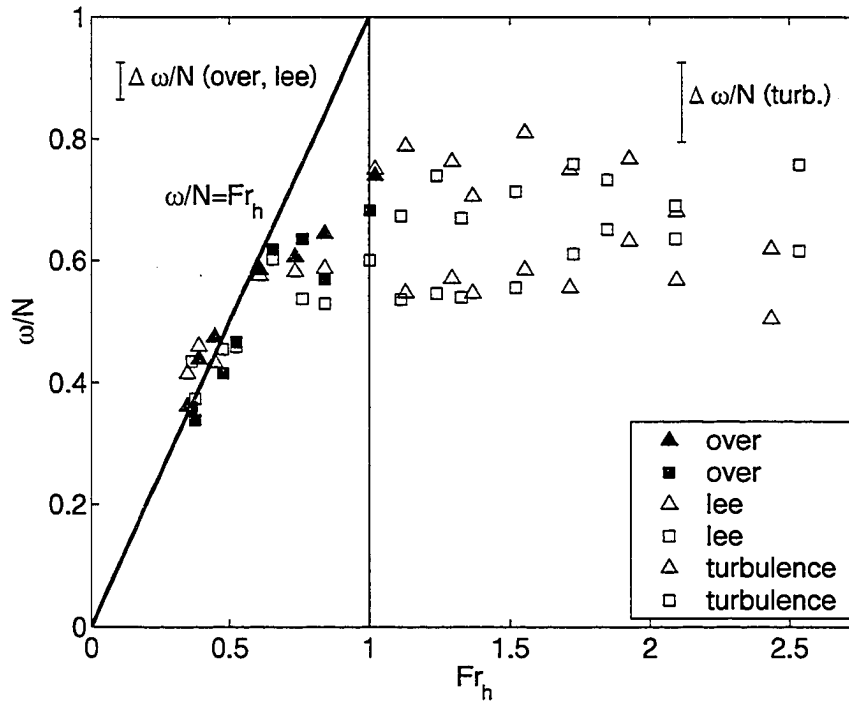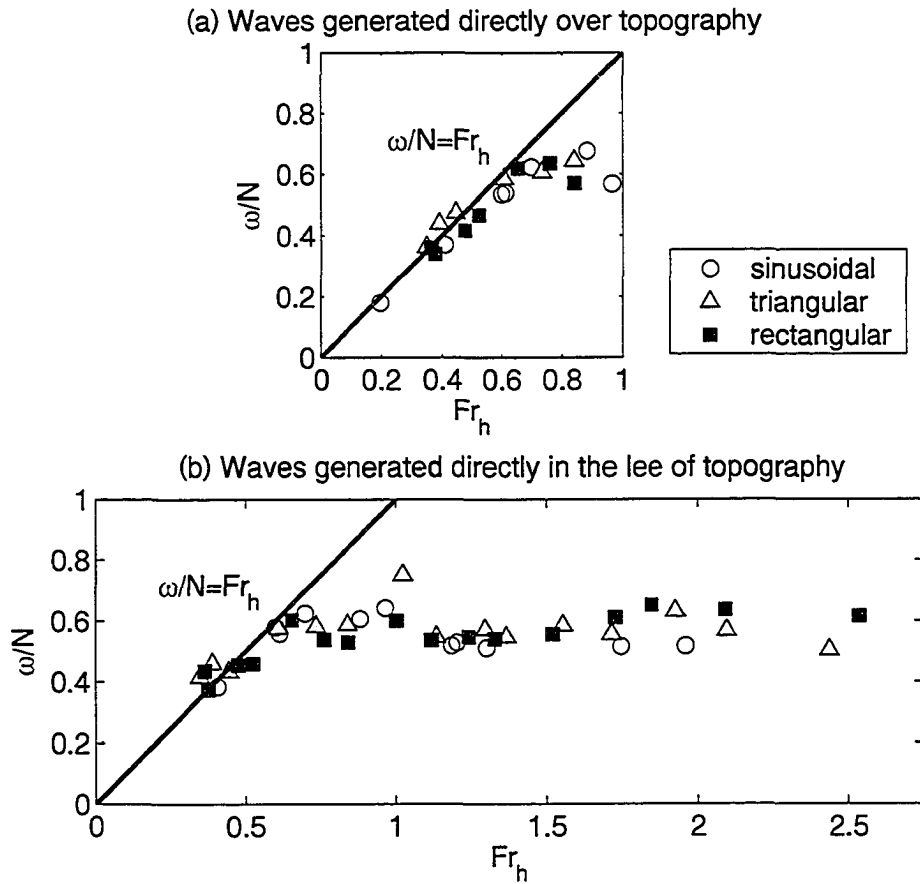
Figure 4.7: Plot of measured relative internal wave frequency, ω/N, as a function of horizontal Froude number, Fr_h, for (a) waves generated directly over and (b) in the lee of large-amplitude sinusoidal and rough topography. The line $\omega/N = \mathrm{Fr}_h$ is plotted to compare the experimental measurements with those predicted by linear theory for smooth hills.

63

iments of Dohan and Sutherland (2003). In their experiments, waves were found to propagate away from a stationary turbulent mixed region at an average frequency of $\omega/N \approx 0.7$. This suggests that the role of the topography in generating smaller-scale waves is to provide a sufficiently rough surface from which vigorous turbulence may be created. The resulting turbulent mixed region then becomes the mechanism of wave generation.

4.3.3 Wave Amplitudes

The amplitudes of the waves are determined in the same way described in Section 2.4 in which the averaging is taken across the windows selected for the power spectral analysis. Figure 4.8 plots the amplitudes of the waves normalized by half the hill height, $2A_\xi/H$, as a function of Fr_h, analogous to Figure 3.8 for the sinusoidal data. As in Figure 4.5, the plot is divided into two regimes by the vertical line, $Fr_h = 1$, the linear theory prediction is included, and the shape and shading of the markers determine the topographic shape and type of wave, respectively.

For $Fr_h < 1$, the waves generated over the hills have amplitudes significantly less than half the hill height, especially for the rectangular hills in which the maximum wave amplitude is only $A_\xi \approx \frac{1}{3}(\frac{H}{2})$. For the triangular hills, the maximum wave amplitude is $A_\xi \approx \frac{1}{2}(\frac{H}{2})$. In both cases, the decreased wave amplitudes are the result of nonlinear effects that change the effective shape of the hill, for example boundary layer separation and subsequent trapping of fluid between the hills. From Figure 4.2, the effective hill height of the rectangular hills is clearly smaller than that of the triangular hills in all cases. In general, the amplitudes of the waves generated over the rectangular and triangular hills satisfy $A_{\xi,\text{rect}} \approx \frac{2}{3}A_{\xi,\text{tri}}$. The rough topography results are compared with those of the large-amplitude sinusoidal hills in Figure 4.9a. The sinusoidal hill data generally lies between that of the rectangular and

64
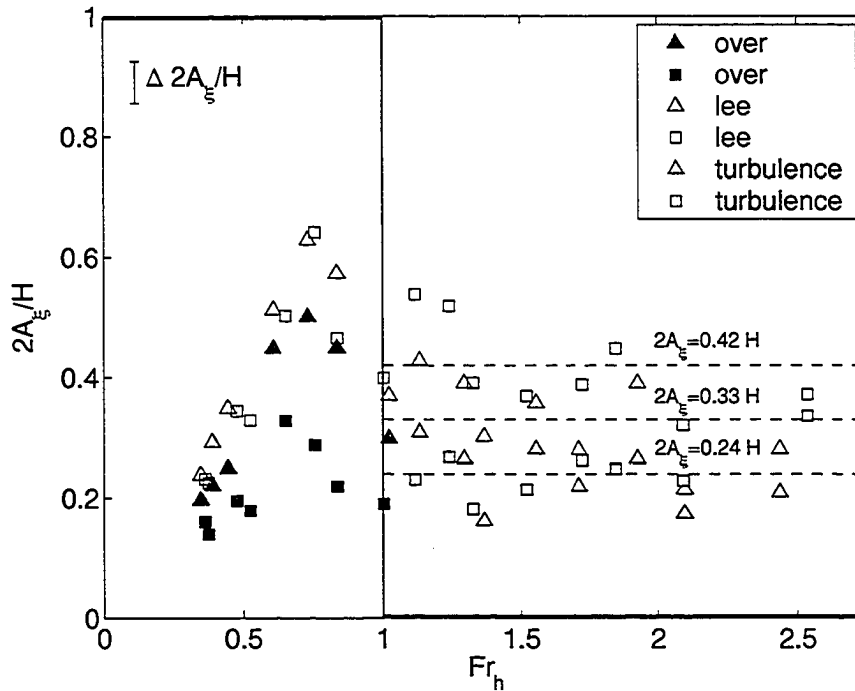
Figure 4.8: Plot of relative internal wave amplitude, $2A_\xi/H$, as a function of Fr_h for the three types of waves generated from rough topography. The thick horizontal lines give the amplitude for linear propagating internal waves. The dashed lines correspond to the average amplitudes of waves generated directly in the lee for $Fr_h > 1$ ($2A_\xi = 0.42H$ for the rectangular data and $0.33H$ for the triangular data) and for the turbulence-generated waves ($2A_\xi = 0.24H$ for the combined rectangular and triangular data).

65

triangular hills, as expected from the qualitative images of flow separation shown in Figures 3.3b,d and 4.2a–d.

Returning to Figure 4.8, for $Fr_h < 1$, the propagating lee wave amplitudes are also plotted and are consistently higher than those of the waves generated over the hills. With the exception of one data point, the lee wave amplitudes are independent of topographic shape. Again, this can be explained qualitatively by comparing the side-by-side images in Figure 4.2. Despite the difference in flow structure directly over the hills, the structure of the boundary-trapped lee wave, in particular its amplitude, is remarkably similar. Combining this observation with the strong coupling between the boundary-trapped and propagating lee waves quantified in the previous section, we might expect the amplitudes to match as well. Figure 4.9b illustrates that the large-amplitude sinusoidal data also matches.

Moving to the regime characterized by $Fr_h > 1$, there are two important observations to be made. First of all, the topographic shape has a small but noticeable effect on the lee wave amplitudes but not on the turbulence-generated (far lee) wave amplitudes. In particular, the average relative lee wave amplitudes for the rectangular and triangular hills are $2A_\xi/H \approx 0.42$ and 0.33, respectively, with $\Delta 2A_\xi/H \approx 0.07$, whereas for the waves generated by the turbulent region, $2A_\xi/H \approx 0.24$ and 0.25, respectively, with $\Delta 2A_\xi/H \approx 0.06$. Second, the relative amplitudes of the propagating lee waves are, in general, larger than those of the turbulence-generated waves.

In terms of the waves generated by the turbulent mixed region, the first observation is consistent with the explanation provided in Section 4.3.2 that the topographic shape is important only insofar as providing a rough surface from which turbulence can be created. Even the name "turbulence-generated" waves, which has been used throughout this report to refer to the waves propagating away from the turbulent mixed region, implies that the specific char-

66

acteristics of the topography are not important.

For the propagating lee waves, however, the topographic shape is important because it affects the structure of the resulting coherent, turbulent boundary-trapped lee wave, and consequently, the propagating internal waves. In particular, we observed in Figure 4.3 that high-speed flow over the rectangular hills resulted in a large patch of turbulence directly over the last hill, which increased the effective height of the lee structure. These growing downstream turbulent patches were, in most cases, not created over the triangular hills. Figure 4.9b further compares these results with those of the large-amplitude sinusoidal hills. The average relative amplitude for the sinusoidal data lies between that of the triangular and rectangular data at $2A_\xi/H \approx 0.39 \pm 0.11$.

In Figure 4.8, the amplitudes of the internal waves were compared to the hill height were larger for the waves generated directly in the lee. If instead we normalize the wave amplitude by the horizontal wavelength, we find that the resulting relative amplitudes of the lee and turbulence-generated waves are comparable. Figure 4.10 plots theses relative amplitudes for experiments with $Fr_h > 1$. These waves are generated by dynamic mechanisms, meaning that they are not directly excited by a solid boundary but are indirectly excited by a pliable flow structure, for example boundary-trapped lee waves and turbulence. The large-amplitude sinusoidal data is also included. From this figure, we observe that the waves are relatively large-amplitude in that the amplitude is approximately 1.5% of the horizontal wavelength and 15% of the breaking amplitude. We also confirm the collapse of the data onto two narrow ranges of propagation angles, $\Theta = 55 \pm 3^o$ ($\omega \approx 0.57N$) for the waves generated by combined flow over envelope topography and boundary-trapped lee waves and $\Theta = 43 \pm 3^o$ ($\omega \approx 0.72N$) for the waves generated by the turbulent mixed region.

These values are consistent with those of other studies involving the dy-
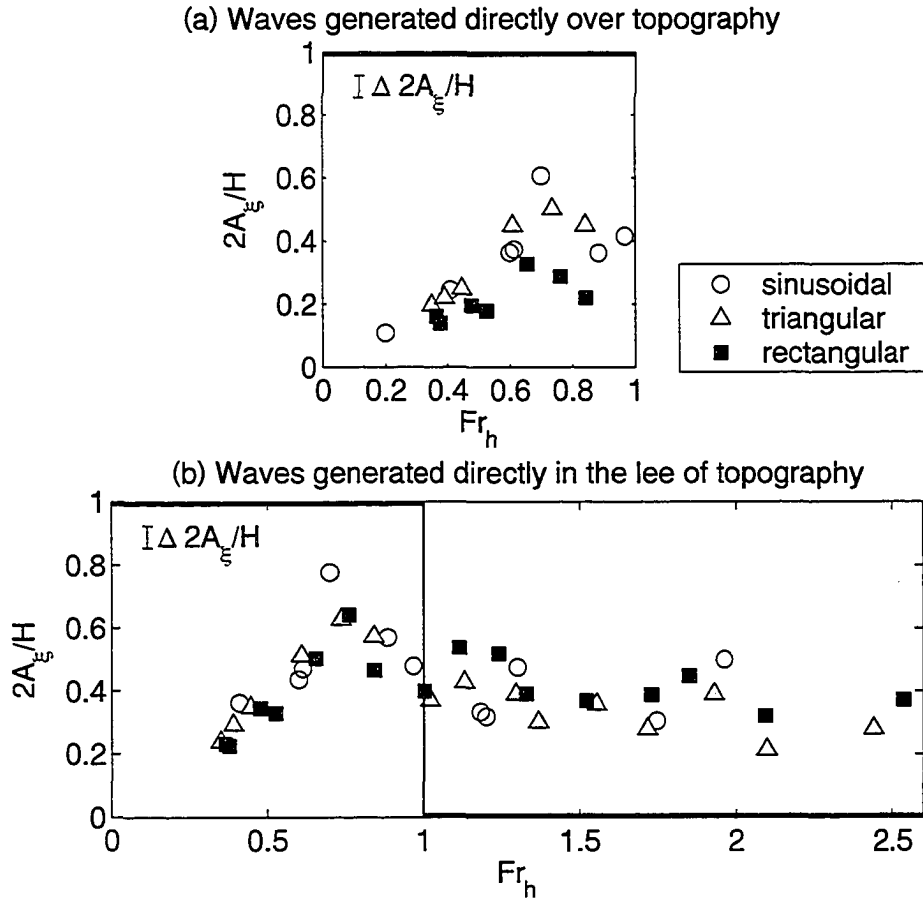
Figure 4.9: Plot of relative internal wave amplitude, $2A_\xi/H$, as a function of horizontal Froude number, Fr_h, for (a) waves generated directly over and (b) in the lee of large-amplitude sinusoidal and rough topography. The thick horizontal lines, $2A_\xi/H = 1$ and $2A_\xi/H = 0$, are plotted to compare the experimental measurements with those predicted by linear theory for smooth hills.

68
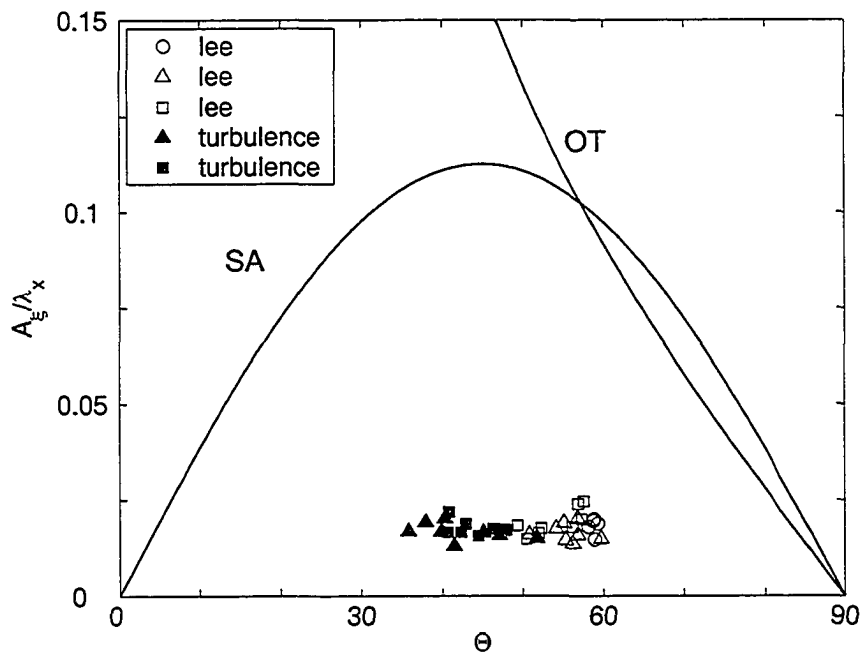
Figure 4.10: Plot of relative wave amplitude, A_ξ/λ_x, as a function wave propagation angle, Θ, for dynamically-generated waves. The curve denoted "SA" is the critical relative amplitude at which the waves should become unstable by self-acceleration. The curve denoted "OT" is the relative amplitude at which the waves should overturn.

69

Table 4.1: Comparison of angle of wave propagation and relative wave amplitude for five studies involving the dynamic generation of internal waves.

Study	Mechanism of wave excitation	Θ ($^\circ$)	A_ξ/λ_x
Linden (1975)	Stationary turbulence	≈ 35	N/A
Dohan and Sutherland (2003)	Stationary turbulence	42 - 55	0.02 - 0.04
Sutherland and Linden (1998)	Turbulent shear flow	46 - 60	0.003 - 0.03
Flynn and Sutherland (2004)	Intrusive gravity current	41 - 64	0.005 - 0.02
Present study (2005)	Boundary-trapped lee waves	52 - 58	0.015 - 0.021
	Turbulence	39 - 47	0.015 - 0.020

namic generation of internal waves, as summarized in Table 4.1. In addition to the similarity of our results to the mixing box experiments of Dohan and Sutherland (2003), our results also match those of Sutherland and Linden (1998) and Flynn and Sutherland (2004), who studied stratified flow past a thin barrier and intrusive gravity currents, respectively. The resulting mechanism of wave generation in both cases involved flow over an undular coherent structure, similar to the flow over boundary-trapped lee waves observed in our experiments.

4.3.4 Blocked Layers Revisited

Throughout this report, we have emphasized the importance of nonlinear effects, such as boundary layer separation, on wave generation. In the case where the boundary layer separates to form stagnant regions of fluid between successive hills, the effect has been to decrease the resulting amplitude of the waves generated above, which consequently decreases the amount of momentum transported by the waves. As discussed previously (Section 3.3.3), the parameter that primarily controls boundary layer separation is Fr_v^{-1}. In this section, we identify critical values of Fr_v^{-1} above which blocking is important

70

for the different topographic shapes studied.

We do this using an analysis similar to that of Welch et al. (2001), who studied the large-scale effects of flow over sinusoidal mesoscale topography using numerical simulations. As a way of presenting their results, they plotted the simulated form drag, F_D, normalized by its value from linear theory, $F_{D,\text{lin}}$, (A.22) as a function Fr_v^{-1} for various simulation parameters. (Note that the form drag is equal to the vertical flux of horizontal momentum, $\mathcal{F}_{uw}$.) They then derived an approximate analytic formula for the drag, which took into account the blocked layer. In particular, they assumed an idealized surface pressure, p'_{ideal}, which equaled exactly zero within the blocked layer and outside the blocked layer, it equaled its value from linear theory, $p' = -\frac{1}{2}\rho_0 UNH^*\sin kx$, where H^* is the effective hill height.

In nondimensional form, the analytic drag, $\hat{F}_{D,\text{blkd}}$, is given by (Welch et al., 2001)

$$
\hat{F}_{D,\text{blkd}} \approx \frac{1}{\pi}\frac{\text{Fr}_v^{-1}*}{\text{Fr}_v^{-1}}\left\{ \cos^{-1}\left[1 - \frac{2\text{Fr}_v^{-1}*}{\text{Fr}_v^{-1}}\right] \right.
$$
$$
\left. - 2\left[1 - \frac{2\text{Fr}_v^{-1}*}{\text{Fr}_v^{-1}}\right]\sqrt{\frac{\text{Fr}_v^{-1}*}{\text{Fr}_v^{-1}} - \left(\frac{\text{Fr}_v^{-1}*}{\text{Fr}_v^{-1}}\right)^2} \right\}, \tag{4.1}
$$

where $\text{Fr}_v^{-1}*$ is the critical value of Fr_v^{-1} above which the effects of blocking act to reduce the linear theory prediction. Based on our results thus far, we would expect the critical value to be lowest for waves generated over the rectangular hills.

Figure 4.11 plots the normalized drag, $F_D/F_{D,\text{lin}}$, as a function of Fr_v^{-1} for all experiments in which $F_{D,\text{lin}}$ is defined, i.e. for $\text{Fr}_h < 1$. Also included are the analytic approximations corresponding to $\text{Fr}_v^{-1}*=0.5$ and 0.75, which fit the data quite well. Similar values have been found by other authors for flow over 2D periodic topography, for example $\text{Fr}_v^{-1}* = 0.77$ (Bell and Thompson, 1980), $\text{Fr}_v^{-1}* = 0.67$ (Kimura and Mannins, 1980) and $\text{Fr}_v^{-1}* \approx 0.5 - 1$ (Welch

71
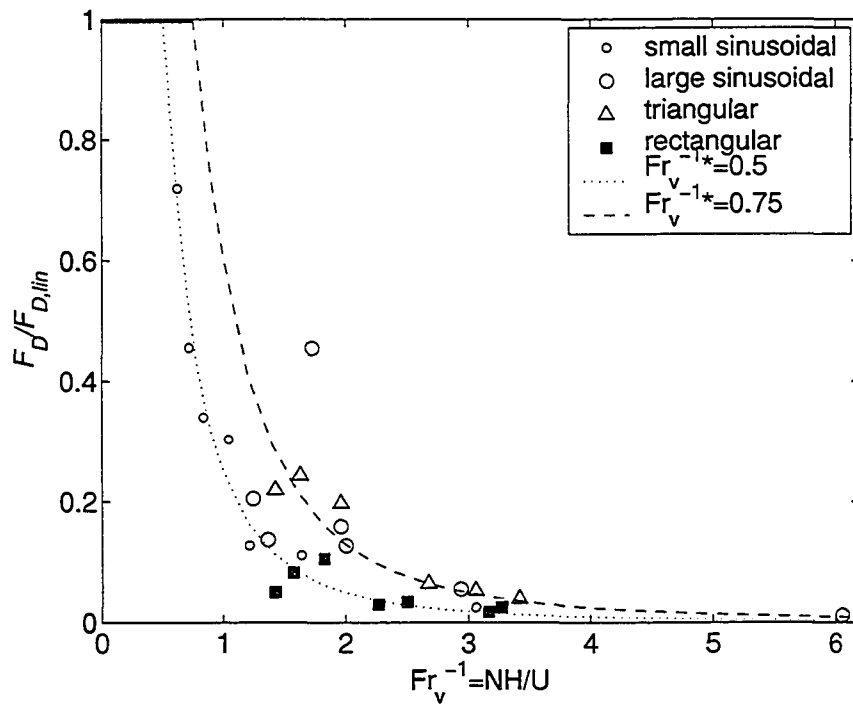
Figure 4.11: Plot of nondimensional form drag, $F_D/F_{D,\text{lin}}$, versus Fr_v^{-1} for all experiments with $\text{Fr}_h < 1$. The thick solid line corresponds to linear theory [Eq. (A.22)], the dotted line to Eq. (4.1) with $\text{Fr}_v^{-1}* = 0.5$, and the dashed line to Eq. (4.1) with $\text{Fr}_v^{-1}* = 0.75$

72

et al., 2001). The rectangular data fit nicely to the curve with $Fr_v^{-1}* = 0.5$, the triangular data to the curve with $Fr_v^{-1}* = 0.75$, and the sinusoidal data somewhere between the two. These results are consistent with our qualitative observations of the relative amounts of fluid trapping between the valleys of the different topographic shapes.

The small- and large-amplitude sinusoidal data are similar for some Fr_v^{-1} values but do not collapse completely. In particular, the large-amplitude data generally correspond to a higher $Fr_v^{-1}*$ value, suggesting that the effective height of the large-amplitude hills is slightly larger than for the small-amplitude hills. In the terminology of Welch et al. (2001), the "dynamic plateau", in which an approximately constant H_{eff} limits the wave amplitudes and other related properties at their source, has not yet been reached. By increasing H further, we should expect H_{eff} to reach an approximately constant value and the data to collapse near the existing large-amplitude sinusoidal data.

4.4 Discussion

The interaction between stratified flow and steep topography is complex. For slower flow speeds ($Fr_h < 1$), the flow can act to modify the shape of the topography, either via flow separation and trapping or by forming turbulent regions above and between the hills. Flow over the effective hill shape mirrors direct topographic forcing over relatively smooth hills. Also at low Fr_h, boundary layer separation from the lee-side slope of the last hill creates boundary-trapped lee waves, flow over which excites propagating internal waves that couple with the boundary-trapped lee waves.

As Fr_h is increased beyond the critical value, $Fr_h \approx 1$, coherent turbulent boundary-trapped lee structures occur and weakly couple with the vertically-propagating lee waves. In addition, a region of vigorous turbulence develops

73

far in the lee of the last hill, from which internal waves propagate at a remarkably constant frequency, $\omega/N \approx 0.72 \pm 5$, and corresponding angle of propagation, $\Theta \approx 43 \pm 3°$. The comparison of our results with other studies reveals some universal trends in the characteristics of waves generated by dynamic mechanisms and thus, increases our understanding of these complex processes. For example, it has been proposed that the narrow frequency range associated with the turbulence-generated waves may be the result of an interaction between the wave field and the turbulent mixed region. In particular, because waves having $\Theta = 45°$ transport the greatest amount of horizontal momentum away from their source for a given U and k_x, they may act most efficiently in modifying the turbulence in a way that enhances their excitation (Dohan, 2004).

Chapter 5

Summary and Conclusions

Stratified flow over finite-amplitude periodic topography generates internal waves via three distinct mechanisms, depending on the topographic shape and flow speed. The first mechanism is that of topographic forcing, whereby fluid flows into and out of the topographic valleys, thus displacing the fluid above and exciting internal waves. If the topography is small-amplitude and smooth and the flow speed satisfies $Fr_h < 1$, then linear theory should give reasonable estimates of wave properties. In our experiments, however, we found that even for our small-amplitude hills with $H/L = 0.1$, linear theory considerably overestimated the internal wave amplitudes and consequently, the momentum fluxes. These quantities are used in environmental models to infer such things as mixing rates in the ocean and changes in mean wind patterns in the atmosphere and thus, it is important to have reliable estimates.

Based on our results, we recommend that for relatively smooth periodic topography having $H/L \approx 0.1$, the linear theory prediction for the wave amplitude be reduced at least to $A_\xi \approx 0.6 \left(\frac{H}{2} \right)$ for $0.6 \lesssim Fr_h < 1$ ($Fr_v^{-1} \lesssim 1$) and even further for smaller Fr_h (and thus, larger Fr_v^{-1}). This is necessary in order to compensate for the nonlinear process of boundary layer separation and consequent flow trapping between the valleys. For larger-amplitude topography, such as our large-amplitude sinusoidal, triangular, and rectangular hills,

75

where flow blocking reduces the effective hill height even more significantly, the estimates should be reduced further. Based on Figure 4.9a, reasonable approximations for $0.6 \lesssim \mathrm{Fr}_h < 1$ are $A_\xi \approx 0.3\left(\frac{H}{2}\right)$, $0.4\left(\frac{H}{2}\right)$, and $0.5\left(\frac{H}{2}\right)$ for the rectangular, sinusoidal, and triangular hills respectively. Again, these approximations should be further reduced for smaller Fr_h (larger Fr_v^{-1}).

The effect of flow blocking on form drag and thus, momentum transport, was also examined. In particular, we found that the analytic formula derived by Welch et al. (2001) and reproduced in Eq. (4.1), reasonably predicted the form drag given appropriate values of $\mathrm{Fr}_v^{-1}*$, between 0.5 and 0.75. Since $\mathrm{Fr}_v^{-1}*$ is the critical value above which blocking effects are important, its value was lower for steeper topographies.

In terms of the wave frequencies, linear theory predictions agreed well with measurements for all topographic shapes up to $\mathrm{Fr}_h \approx 0.7$, above which wave frequencies decreased significantly. It may be surprising that the predictions of linear theory could be applied at all to such tall and steep topographic shapes. However, our observations of flow over and between the hills revealed that the effective shape of the steep topography was, in most cases, smoothed by the flow and so resembled flow over relatively smooth periodic hills.

Apart from topographic forcing, our experiments support the mechanism of wave generation via flow over boundary-trapped lee waves, as first introduced by Sutherland (2002). For sufficiently tall topography, in our cases those having $H/L = 0.2$, boundary-trapped lee waves were observed at all tow speeds and strongly coupled with vertically-propagating internal waves for $\mathrm{Fr}_h < 1$. When $\mathrm{Fr}_h > 1$, the flow in the lee of the topography (both small- and large-amplitude) became turbulent. Even so, coherent turbulent structures were shed in the lee, above which internal waves were excited. The frequencies of both waves were within a relatively narrow range, with slightly larger values for the boundary-trapped lee waves. This is similar to the observations of

76

coherent turbulent structures shed in the lee of a thin barrier, below which internal waves propagated with the same length-scale and horizontal phase speed as the disturbances (Sutherland and Linden, 1998). In our experiments, the mechanism of wave generation is likely a combination of flow over the coherent boundary-trapped lee waves and over envelope topography, which treats the group of hills as a single unit.

The third and final mechanism of wave generation from stratified flow over finite-amplitude topography is that of vigorous turbulence, which is generated far in the lee of rough topography, for example our triangular and rectangular hills. As in other studies involving wave generation from turbulence, the internal waves propagated away from the turbulent mixed region within a narrow range of propagation angles near $\Theta = 45^o$, despite the many scales that should be expected from turbulence. Waves propagating at such angles transport horizontal momentum away from their source at the maximum rate (see A.4, Page 88). This is of particular interest in the atmosphere where the deposition of momentum greatly affects mean winds and consequently, local weather predictions and aviation safety.

It is difficult to apply our results directly to the ocean because most of the available data is in the form of average statistics of the internal tides, which are dominated by the lowest vertical wavenumbers and near-inertial frequencies. All other internal wave activity, including the smaller-scale waves generated in our experiments, is regarded as random fluctuations. Nonetheless, these random fluctuations form part of the internal wave spectrum in the ocean and contribute to ocean mixing at the small-scales.

Bibliography

Baines, P. G. (1995). *Topographic Effects in Stratified Flows*. Cambridge University Press.

Baines, P. G. and K. P. Hoinka (1985). Stratified flow over two-dimensional topography in fluid of infinite depth: A laboratory simulation. *J. Atmos. Sci. 42*, 1614–1630.

Balmforth, N. J., G. R. Ierley, and W. R. Young (2002). Tidal conversion by subcritical topography. *J. Phys. Ocean. 32*, 2900–2914.

Bell, R. C. and R. O. Thompson (1980). Valley ventilation by cross winds. *J. Fluid Mech. 96*, 757–767.

Boyer, D. L. and A. Srdic-Mitrovic (2002). Laboratory studies of continuously stratified flows past obstacles. In R. Grimshaw (Ed.), *Environmental Stratified Flows*, pp. 191–222. Kluwer.

Braun, S. A., R. Rotunno, and J. B. Klemp (1999). Effects of coastal orography on landfalling cold fronts. part i: Dry, inviscid dynamics. *J. Atmos. Sci. 56*, 517–533.

Carruthers, D. J. and J. C. R. Hunt (1986). Velocity fluctuations near an interface between a turbulent region and a stably stratified layer. *J. Fluid Mech. 165*, 475–501.

Dalziel, S. B., G. O. Hughes, and B. R. Sutherland (2000). Whole field density measurements. *Expt. Fluids 28*, 322–335.

Dohan, K. (2004). *Internal Wave Generation from a Turbulent Mixed Region.* Ph. D. thesis, University of Alberta.

Dohan, K. and B. R. Sutherland (2003). Internal waves generated from a turbulent mixed region. *Phys. Fluids 15*, 488–498.

Flynn, M. R. and B. R. Sutherland (2004). Intrusive gravity currents and internal gravity wave generation in stratified fluid. *J. Fluid Mech. 514*, 355–383.

Garabato, A. C. N., K. L. Polzin, B. A. King, K. J. Heywood, and M. Visbeck (2004). Widespread intense turbulent mixing in the southern ocean. *Science 303*(5655), 210–213.

Kimura, F. and P. Mannins (1980). Blocking in periodic valleys. *Bound.-Layer Meteor. 44*, 137–169.

Klymak, J. M. and M. C. Gregg (2004). Tidally generated turbulence over the knight inlet sill. *J. Phys. Ocean. 34*(5), 1135–1151.

Laprise, R. and W. R. Peltier (1989). On the structural characteristics of steady finite-amplitude mountain waves over bell-shaped topography. *J. Atmos. Sci. 46*(4), 486–495.

Ledwell, J. R., E. T. Montgomery, K. L. Polzin, L. C. S. Laurent, R. W. Schmitt, and J. M. Toole (2000). Evidence of enhanced mixing over rough topography in the abyssal ocean. *Nature 403*, 179–182.

Linden, P. F. (1975). The deepening of a mixed layer in a stratified fluid. *J. Fluid Mech. 71*, 385–405.

79

Llewellyn Smith, S. G. and W. R. Young (2002). Conversion of the barotropic tide. *J. Phys. Ocean.* *32*, 1554–1566.

Long, R. R. (1953). Some aspects of the flow of stratified fluids. a theoretical investigation. *Tellus 5*, 42–58.

McFarlane, N. A. (1987). The effect of orographically excited gravity wave drag on the general circulation of the lower stratosphere and troposphere. *J. Atmos. Sci. 44*, 1775–1800.

McLandress, C. (1998). On the importance of gravity waves in the middle atmosphere and their parameterizations in general circulation models. *J. Atmos. Solar-Terres. Phys. 60*(14), 1357–1383.

Muraki, D. J. (2005). A modern look at the theories of Lyra and Long on 2D topographic flow. *J. Atmos. Sci.*, in preparation.

New, A. L. and J. C. B. DaSilva (2002). Remote-sensing evidence for the local generation of internal soliton packets in the central bay of biscay. *Deep Sea Res. I 49*(5), 915–934.

Oster, G. (1965). Density gradients. *Scientific American 213*, 70.

Rudnick, D. L., T. J. Boyd, R. E. Brainard, G. S. Carter, G. D. Egbert, M. C. Gregg, P. E. Holloway, J. M. Klymak, E. Kunze, C. M. Lee, M. D. Levine, D. S. Luther, J. P. Martin, M. A. Merrifield, J. N. Moum, J. D. Nash, R. Pinkel, L. Rainville, and T. B. Sanford (2003). From tides to mixing along the hawaiian ridge. *Science 301*(5631), 355–357.

Scinocca, J. F. and W. R. Peltier (1989). Pulsating downslope windstorms. *J. Atmos. Sci. 46*, 2885–2914.

Skyllingstad, E. D. and D. W. Denbo (1994). The role of internal gravity waves in the equatorial current system. *J. Phys. Ocean. 24*, 2093–2110.

Spiegel, E. and G. Veronis (1960). On the boussinesq approximation for a compressible fluid. *The Astrophysical Journal 131*, 442–447.

St. Laurent, L. and C. Garrett (2002). The role of internal tides in mixing the deep ocean. *J. Phys. Ocean. 32*, 2882–2899.

St. Laurent, L., S. Stringer, C. Garrett, and D. Perrault-Joncas (2003). The generation of internal tides at abrupt topography. *Deep Sea Res. I 50*(8), 987–1003.

Staquet, C. and J. Sommeria (2002). Internal gravity waves: From instabilities to turbulence. *Ann. Rev. Fluid Mech. 34*, 559–593.

Sutherland, B. R. (2001). Finite-amplitude internal wavepacket dispersion and breaking. *J. Fluid Mech. 429*, 343–380.

Sutherland, B. R. (2002). Large-amplitude internal wave generation in the lee of step-shaped topography. *Geophys. Res. Lett. 29*(16). doi:10.1029/2002GL015321.

Sutherland, B. R., S. B. Dalziel, G. O. Hughes, and P. F. Linden (1999). Visualization and measurement of internal waves by synthetic schlieren. part 1: Vertically oscillating cylinder. *J. Fluid Mech. 390*, 93–126.

Sutherland, B. R. and P. F. Linden (1998). Internal wave excitation from stratified flow over a thin barrier. *J. Fluid Mech. 377*, 223–252.

Welch, W., P. Smolarkiewicz, R. Rotunno, and B. A. Boville (2001). The deepening of a mixed layer in a stratified fluid. *J. Atmos. Sci. 58*(12), 1477–1492.

Appendix A

Linear Internal Wave Theory

A.1 Introduction

The theory of linear internal waves is used extensively in this report and thus, it is necessary to give a detailed description of what it entails. In its most general use, the term "linear theory", refers to a set of linearized partial differential equations describing the motion of internal waves. This section provides a derivation of these equations and the important results that follow from the solution.

A.2 Equations of Fluid Motion

The study of any fluid motion, including the motion of internal waves, begins with two governing equations: the Navier-Stokes equation, expressing conservation of momentum, and the continuity equation, expressing conservation of mass.

The Navier-Stokes equation is written

$$\rho_T \frac{D\boldsymbol{u}}{Dt} = -\nabla p_T + \rho_T \boldsymbol{g} + \mu \nabla^2 \boldsymbol{u}, \qquad (A.1)$$

where ρ_T is the total density of the fluid, $\boldsymbol{u} = (u, v, w)$ denotes the components of the velocity field in the $\hat{x}$, $\hat{y}$, and $\hat{z}$ directions respectively, p_T is the pressure, $\boldsymbol{g} = -g\hat{z}$ is the acceleration due to gravity, and μ is the molecular viscosity.

82

The material derivative,

$$\frac{D}{Dt} \equiv \frac{\partial}{\partial t} + \boldsymbol{u} \cdot \nabla, \tag{A.2}$$

introduces nonlinearity through the term $\boldsymbol{u} \cdot \nabla = u\frac{\partial}{\partial x} + v\frac{\partial}{\partial y} + w\frac{\partial}{\partial z}$.

The continuity equation is written

$$\frac{D\rho_T}{Dt} = -\rho_T \nabla \cdot \boldsymbol{u}. \tag{A.3}$$

If we assume that the flow is incompressible, which is a good assumption for the ocean and a reasonable assumption for scales smaller than ten kilometers (a scale height) in the atmosphere, then

$$\frac{D\rho_T}{Dt} = 0 \tag{A.4}$$

and consequently we have

$$\nabla \cdot \boldsymbol{u} = 0. \tag{A.5}$$

Equations (A.1), (A.4), and (A.5) comprise a set of five partial differential equations in five unknowns (u, v, w, ρ_T, p_T). These equations describe a wide range of flow phenomena, including waves and turbulence occurring on length scales as large as thousands of kilometers and as small as millimeters.

In this study we focus on applications in the ocean and lower atmosphere involving internal waves with length scales ranging from 10 to 1000 meters. For such waves, several simplifications can be made to the governing equations. To begin, for such large Reynolds number flows, the effects of viscosity can be ignored, except near boundary layers. This allows us to set $\mu = 0$ in (A.1).

We next assume that the flow is "Boussinesq", meaning that density variations are only important as they affect the buoyancy term, $\rho_T g$, in (A.1). Boussinesq internal waves exist in fluids whose density decreases by only a small fraction of the total density change with height. This is suitable for a study of the ocean, in which the density changes by less than 10% from the surface to the ocean floor. In the atmosphere, the approximation is useful

83

only over scales less than the scale height (Spiegel and Veronis, 1960). Use of the Boussinesq approximation further simplifies (A.1) by setting $\rho_T = \rho_0$, a constant, in all terms except the buoyancy term.

We further simplify the equations by subdividing the density and pressure fields into background fields, $\overline{\rho}(z)$ and $\overline{p}(z)$, and perturbation fields, $p(x,t)$ and $\rho(x,t)$. That is,

$$\rho_T(x,t) = \overline{\rho}(z) + \rho(x,t)$$
$$p_T(x,t) = \overline{p}(z) + p(x,t)$$

(A.6)

and we assume that the background fields are in hydrostatic balance, satisfying

$$\frac{d\overline{p}}{dz} = -\overline{\rho}g.$$

(A.7)

Substituting equations (A.6) and (A.7) into (A.1) and incorporating the assumptions thus far reduces (A.1) and (A.4) to

$$\rho_0 \frac{Du}{Dt} = -\nabla p - \rho g$$

(A.8)

$$\frac{D\rho}{Dt} + w\frac{d\overline{\rho}}{dz} = 0.$$

(A.9)

If we make the final assumption that the waves are small-amplitude, then the nonlinear terms in the material derivative may be neglected. In particular, if there is no mean background flow then $\frac{D}{Dt} \rightarrow \frac{\partial}{\partial t}$. The final result is the linearized system of five equations in five unknowns:

$$\rho_0 \frac{\partial u}{\partial t} = -\frac{\partial p}{\partial x}$$

(A.10)

$$\rho_0 \frac{\partial v}{\partial t} = -\frac{\partial p}{\partial y}$$

(A.11)

$$\rho_0 \frac{\partial w}{\partial t} = -\frac{\partial p}{\partial z} - \rho g$$

(A.12)

$$\frac{\partial \rho}{\partial t} + w\frac{d\overline{\rho}}{dz} = 0$$

(A.13)

$$\frac{\partial u}{\partial x} + \frac{\partial v}{\partial y} + \frac{\partial w}{\partial z} = 0.$$

(A.14)

84

A.3 Solution to Linearized Equations and Dispersion Relation

The solution to the linearized equations of the previous section provides insight into the properties of small-amplitude internal waves, including the dispersion relation, the relationships between the components of the velocity field and the perturbation density field, and the energy and momentum transport. To obtain the solution, we rewrite equations (A.10) through (A.14) in matrix form:

$$
\begin{pmatrix}
\frac{\partial}{\partial t} & 0 & 0 & 0 & \frac{1}{\rho_0}\frac{\partial}{\partial x} \\
0 & \frac{\partial}{\partial t} & 0 & 0 & \frac{1}{\rho_0}\frac{\partial}{\partial y} \\
0 & 0 & \frac{\partial}{\partial t} & \frac{g}{\rho_0} & \frac{1}{\rho_0}\frac{\partial}{\partial z} \\
0 & 0 & -\frac{\rho_0}{g}N^2 & \frac{\partial}{\partial t} & 0 \\
\frac{\partial}{\partial x} & \frac{\partial}{\partial y} & \frac{\partial}{\partial z} & 0 & 0
\end{pmatrix}
\begin{pmatrix} u \\ v \\ w \\ \rho \\ p \end{pmatrix} = 0.
\tag{A.15}
$$

In the above equation, the $\frac{d\bar{\rho}}{dz}$ term of equation (A.13) is written in terms of the buoyancy frequency, N, using the definition:

$$
N^2 = -\frac{g}{\rho_0}\frac{d\bar{\rho}}{dz}.
\tag{A.16}
$$

For non-trivial solutions, the determinant of the matrix in equation (A.15) must be zero. That is

$$
\left[\frac{\partial^3}{\partial t^3}\nabla^2 + N^2\nabla_H{}^2\frac{\partial}{\partial t}\right]b = 0,
\tag{A.17}
$$

where b is one of the five unknowns (u, v, w, ρ, p) and $\nabla_H \equiv (\frac{\partial}{\partial x}, \frac{\partial}{\partial y})$. We assume periodic solutions of the form

$$
b(x, y, z, t) = A_b \exp[i(k_x x + k_y y + k_z z - \omega t)],
\tag{A.18}
$$

where (k_x, k_y, k_z) are the components of the wave number vector, $\boldsymbol{k}$, and it is understood that the actual wave structure is given by the real part of b. Substituting (A.18) into (A.17) gives $-i\omega^3(k_x^2 + k_y^2 + k_z^2) + N^2 i\omega(k_x^2 + k_y^2) = 0$.

85

Taking only non-stationary solutions yields the dispersion relation:

$$\omega = N \frac{\sqrt{k_x^2 + k_y^2}}{\sqrt{k_x^2 + k_y^2 + k_z^2}} = N \cos \Theta, \qquad (A.19)$$

where Θ is the angle that $\boldsymbol{k}$ makes with the horizontal, or equivalently, the angle to the vertical at which waves propagate.

The dispersion relation illustrates an important property of internal waves: the frequency of propagating internal waves cannot exceed the buoyancy frequency. Waves generated with frequencies $\omega > N$ exponentially decay from their source and are termed "evanescent waves".

A.4 Properties of Linear Internal Waves

Many properties of internal waves can be described in terms of the frequency and wavenumber. For the remainder of this section, we will assume two-dimensional waves in the $x - z$ plane. Such waves are representative of the waves generated in the laboratory experiments.

The phase velocity gives the speed and direction at which lines of constant phase move. It is defined by

$$\boldsymbol{c}_p = \frac{\omega}{|\boldsymbol{k}|} \frac{\boldsymbol{k}}{|\boldsymbol{k}|} = \frac{\omega}{k_x^2 + k_z^2} (k_x, k_z). \qquad (A.20)$$

The group velocity is the velocity of wave packets and energy transport. It is defined by

$$\boldsymbol{c}_g = \left(\frac{\partial \omega}{\partial k_x}, \frac{\partial \omega}{\partial k_z} \right) = \frac{N}{(k_x^2 + k_z^2)^{\frac{3}{2}}} (k_z^2, -k_x k_z). \qquad (A.21)$$

It is interesting to note that $\boldsymbol{c}_p \cdot \boldsymbol{c}_g = 0$, indicating that the direction of phase movement is perpendicular to the direction of energy transport.

The vertical displacement field, ξ, is defined implicitly through the relation $w = \frac{\partial \xi}{\partial t}$ and can be written in the form given in (A.18). That is,

$$\xi = A_\xi \exp[i(k_x x + k_z z - \omega t)].$$

86

Table A.1: Relations between basic state fields and the vertical displacement field. Also included are the relations for the streamfunction (ψ), the change in squared buoyancy frequency (ΔN^2) and its time derivative (N_t^2).

Field variable: b	Complex amplitude: A_b
ξ	A_ξ
$w = \frac{\partial \xi}{\partial t}$	$A_w = -i\omega A_\xi$
$\frac{\partial \psi}{\partial x} = w$	$A_\psi = -\frac{\omega}{k_x} A_\xi$
$u = -\frac{\partial \psi}{\partial z}$	$A_u = i\omega \frac{k_z}{k_x} A_\xi$
$\rho = -\frac{d\bar{\rho}}{dz}\xi$	$A_\rho = \frac{\rho_0}{g} N^2 A_\xi$
$\frac{\partial p}{\partial x} = -\rho_0 \frac{\partial u}{\partial t}$	$A_p = i\omega^2 \rho_0 \frac{k_z}{k_x^2} A_\xi$
$\Delta N^2 = -\frac{g}{\rho_0}\frac{\partial \rho}{\partial z}$	$A_{\Delta N^2} = -ik_z N^2 A_\xi$
$N_t^2 = \frac{\partial}{\partial t}(\Delta N^2)$	$A_{N_t^2} = k_z \omega N^2 A_\xi$

The amplitudes of the other field variables can be written in terms of A_ξ using the basic defining equations for each variable. For example, to determine A_w we use the relation,

$$w = \frac{\partial \xi}{\partial t} = -i\omega A_\xi \exp[i(k_x x + k_z z - \omega t)],$$

from which it follows that

$$A_w = -i\omega A_\xi.$$

The remaining relations are summarized in Table A.4, including those for the streamfunction (ψ), the change in the squared buoyancy frequency (ΔN^2) and its time derivative (N_t^2). The latter quantity, N_t^2, is used extensively in our analyses of internal waves.

Two properties of internal waves that are of particular interest are the momentum and energy fluxes. The vertical flux of horizontal momentum $\mathcal{F}_{uw}$ is defined in terms of the cross-correlation, $\langle uw \rangle$, where the angled brackets

87

denote averaging over one period of oscillation. Explicitly,

$$
\begin{aligned}
\mathcal{F}_{uw} = \rho_0 \langle uw \rangle &= \frac{\rho_0}{T} \int_0^T uw \, dt \\
&= \frac{\rho_0}{T} \int_0^T A_u \cos(k_x x + k_z z - \omega t) \, A_w \cos(k_x x + k_z z - \omega t) \, dt \\
&= \frac{1}{2} \rho_0 A_u A_w \\
&= \frac{1}{4} \rho_0 N^2 \sin(2\Theta) A_\xi^2.
\end{aligned}
$$

$$(A.22)$$

The above expression indicates that waves with $\Theta = 45^o$ and fixed A_ξ transport the greatest momentum.

The energy associated with the waves is in the form of kinetic and potential energy. The average kinetic energy per unit volume, KE, is:

$$
\begin{aligned}
KE &= \frac{1}{2} \rho_0 \langle u^2 + w^2 \rangle \\
&= \frac{1}{4} \rho_0 N^2 A_\xi^2
\end{aligned}
$$

$$(A.23)$$

The average potential energy per unit volume, PE, is defined:

$$
PE = -\frac{1}{2} \langle \rho g \xi \rangle,
$$

$$(A.24)$$

where

$$
\xi = -\frac{\rho}{\frac{d\bar{\rho}}{dz}} = -\rho \frac{g}{\rho_0 N^2}.
$$

This gives:

$$
\begin{aligned}
PE &= \frac{1}{2} \frac{g^2}{\rho_0 N^2} \langle \rho^2 \rangle \\
&= \frac{1}{4} \rho_0 N^2 A_\xi^2 \\
&= KE.
\end{aligned}
$$

$$(A.25)$$

Thus, the total energy per unit volume is $E = 2KE = 2PE$. The vertical flux of energy per unit horizontal area, $\mathcal{F}_{Ez}$, carried by waves of amplitude A_ξ is:

$$
\begin{aligned}
\mathcal{F}_{Ez} &= E c_{g_z} \\
&= \frac{1}{2} \rho_0 N^3 A_\xi^2 \frac{k_x k_z}{(k_x^2 + k_z^2)^{\frac{3}{2}}}.
\end{aligned}
$$

$$(A.26)$$

88

For fixed k_x, we can write

$$\mathcal{F}_{Ez} = \frac{1}{2}\frac{\rho_0 N^3 A_\xi^2}{k_x}\sin(\Theta)\cos^2(\Theta), \qquad (A.27)$$

which has a maximum for $\Theta = \tan^{-1}(\frac{1}{\sqrt{2}}) \simeq 35^\circ$.

89

Appendix B

Derivation of Long's Model

In this chapter, we present the derivation of Long's model for inviscid, free-slip flow over finite-amplitude hills. Explicitly, Long's model for steady, two-dimensional flow of uniformly stratified fluid, characterized by constant buoyancy frequency N_0, moving with uniform upstream speed, U_0, over topography is given by the Helmholtz equation

$$\psi_{xx} + \psi_{zz} + \left(\frac{N_0}{U_0}\right)^2 \psi = 0, \qquad (B.1)$$

in which ψ is the perturbation streamfunction and the subscripts denote partial derivatives. Although (B.1) is a linear partial differential equation, it nonetheless describes finite-amplitude effects, which enter through the specification of nonlinear boundary conditions. In particular, assuming an inviscid, free-slip lower boundary, we require that the surface is itself a streamline, which arbitrarily we set to zero. Thus we require

$$-U_0 h(x) + \psi(x, h(x)) = 0, \qquad (B.2)$$

in which we have evaluated the background streamfunction, $\Psi(z) \equiv -U_0 z$, and the perturbation streamfunction, $\psi(x, z)$, at the height of the topography, $z = h(x)$.

For the generation of small-amplitude, hydrostatic internal waves, equa-

90

tions (B.1) and (B.2) may be solved by standard Fourier methods:

$$\psi(x,z) = \int_{-\infty}^{\infty} \eta(k)e^{i[kx+m(k)z]}\,dk \tag{B.3}$$

in which $m^2 = -k^2 + N_0{}^2/U_0{}^2$ (with the appropriate branch cut taken when computing m so that waves are outward propagating), and $\eta(k)$ is found from the linearized boundary condition

$$U_0 h(x) \simeq \psi(x,0) = \int_{-\infty}^{\infty} \eta(k)e^{ikx}\,dk. \tag{B.4}$$

For large-amplitude disturbances, assuming the streamfunction ψ retains the form in (B.3), the exact boundary condition is

$$U_0 h(x) = \int_{-\infty}^{\infty} \eta(k)e^{i[kx+m(k)h(x)]}\,dk. \tag{B.5}$$

This is a Fredholm integral equation of the first kind that determines the Fourier coefficients $\eta(k)$ from the topographic profile $h(x)$. Generically, first-kind integral equations are ill-conditioned and, consequently, numerical discretization leads to large linear systems whose matrices are poorly conditioned. Nonetheless, if the flow is nearly hydrostatic ($Fr_h \ll 1$), reasonable numerical solutions can be obtained by a direct linear solution method or by Fourier iteration. In nonhydrostatic cases, the ill-conditioning cannot be overcome and a different numerical approach is necessary. Recently, Muraki (2005) has recast Long's model into an integral equation of the second-kind. Numerical discretization of second-kind problems yield matrices which are typically diagonally dominant and thus are better conditioned.

91